

# High Resolution HI observations of the Western Magellanic Bridge

E. Muller<sup>1,2</sup>, L. Staveley-Smith<sup>2</sup>, W. Zealey<sup>1</sup>, S. Stanimirović<sup>3</sup>

<sup>1</sup>University of Wollongong, Northfields Ave. Wollongong, NSW 2500, Australia

<sup>2</sup>Australia Telescope National Facility, CSIRO, PO Box 76, Epping, N.S.W. 1710, Australia

<sup>3</sup>Arecibo Observatory, HC3 Box 53995, Arecibo, Puerto Rico 00612

arXiv:astro-ph/0210615v1 29 Oct 2002

## ABSTRACT

The 21cm line emission from a  $7 \times 6$  degree region, east of and adjoining the Small Magellanic Cloud (SMC) has been observed with the Australia Telescope Compact Array and the Parkes telescopes. This region represents the westernmost part of the Magellanic Bridge, a gas-rich tail extending  $\sim 14$  degrees to the Large Magellanic Cloud (LMC). A rich and complex neutral hydrogen (HI) structure containing shells, bubbles and filaments is revealed. On the larger scale, the HI of the Bridge is organised into two velocity components. This bimodality, which appears to originate in the SMC, converges to a single velocity component within the observed region. A census of shell-like structures suggests a shell population with characteristics similar to that of the SMC. The mean kinematic age of the shells is  $\sim 6$  Myr, in agreement with the SMC shell population, but not with ages of OB clusters populating the Magellanic Bridge, which are approximately a factor of three older. In general, the projected spatial correlation of Bridge HI shells with OB associations is poor and as such, there does not appear to be a convincing relationship between the positions of OB associations and that of expanding spherical HI structures. This survey has found only one HI shell that has an identifiable association with a known H $\alpha$  shell. The origin of the expanding structures is therefore generally still uncertain, although current theories regarding their formation include gravitational and pressure instabilities, HVC collisions and ram pressure effects.

**Key words:** ISM:Bubbles - ISM:Structure - Galaxies:Magellanic Clouds

## 1 INTRODUCTION

The Magellanic Bridge is a loosely defined column of gas, comprising mostly neutral hydrogen, found between the Small and Large Magellanic Clouds (SMC and LMC respectively). The Bridge was discovered originally through 21cm observations by Hindman et al. (1961), and has been mapped in the HI line at increased spatial resolution by Mathewson, Cleary & Murray (1974), and at increased velocity resolution by McGee & Newton (1986). The most recent HI observations are presented by Putman (1998), and Brüns, Kerp & Staveley-Smith (2000).

The tidal influence of the Magellanic Clouds on each other is widely considered to be the mechanism responsible for the development of the Magellanic Bridge (eg. Putman 2000; Demers & Battinelli 1998; Staveley-Smith et al. 1998), and has been modelled as such through numerical simulations (eg. Gardiner, Sawa & Fujimoto 1994; Gardiner & Noguchi 1996; and Sawa, Fujimoto & Kumai 1999). The simulations suggest that formation of the Bridge may have be-

gun during the most recent of a series of close Cloud/Cloud interactions, around 200 Myr ago. Zaritsky et al. (2000) suggest that the SMC may also have been subject to a period of ram pressure, and have measured a shift in the centre of the young blue population relative to that of the older population. The degree to which this hydrodynamic effect has influenced the evolution of the Magellanic System has not yet been quantified.

Studies of the morphology of the HI in the SMC have been made by a few groups: HI shells have been identified and catalogued by Staveley-Smith et al. (1997) and by Stanimirović et al. (1999). The statistical properties of the Interstellar Medium (ISM) have been studied by Stanimirović et al. (1999), Stanimirović (2000) and Stanimirović & Lazarian (2001). The shell population, its evolution and relationship with star forming regions is studied by Oey & Clarke (1997). These statistical studies lead to comparisons that can assist in the understanding of the shell evolutionary environment for these systems. Studies of the HI shell population in other galaxies have been used as a probe into the physical pro-

cesses active in the local ISM; Puche et al. (1992) compiled a catalogue of the shells in the Magellanic type galaxy Holmberg II (HoII), while Walter & Brinks (2001) have made similar observations of the shell population of the Magellanic type DDO 47 galaxy. Wilcots & Miller (1998) made a high-resolution study of the HI in the dwarf irregular galaxy IC10, and found that it is dominated by a rather chaotic and frothy HI morphology.

Further observations and analysis of the HI shell population of HoII designed to test the standard 'stellar wind' mechanism of shell generation (Rhode et al. 1999) have shown that there are observational inconsistencies with this idea. Alternative shell mechanisms, such as gamma ray bursts and high velocity cloud (HVC) impacts have been proposed by these authors. Other suggestions for the formation of these HI holes by ram pressure have been made by Bureau & Carnigan (2002). An examination of the shell population of the Galaxy (Ehlerova & Palous, 1996) suggests that the formation of these shells is more likely to be the product of stellar wind, rather than collisions with HVCs.

We present here high spatial and velocity resolution observations of the Magellanic Bridge, conducted with both the Australia Telescope Compact Array (ATCA) and with the Parkes telescope <sup>\*</sup>. The combined data cube is sensitive to structure on all angular scales between 98 arcsec and  $\sim 6$  degrees. A survey for shells and bubbles in the observed volume has been made, and statistical analysis is compared with that of the SMC and with the HoII shell survey by Puche et al. (1992).

Section 2.1 and Section 2.2 outline the procedures involved in the observations made with the ATCA and with the Parkes telescope, while Section 2.3 outlines the methods used in merging these two datasets. Section 2.4 discusses the general appearance and highlights some of the more dramatic features of the HI cube. The shell selection criteria are defined in Section 3. Section 3.1 contains a statistical summary of the results and in Section 4 we present a study of the correlation of the shell and OB association population of the Bridge. In Section 5 we compare an HI shell found from this study with an H $\alpha$  region found already within the Bridge. Limitations affecting the shell survey are discussed in Section 6. Section 7 contains a discussion of the stellar wind model, as applied to the Magellanic Bridge shell population, as well as a comparison with the energetics of the SMC shell population. Alternative shell generation mechanisms are discussed in Section 8, and we summarise our findings in Section 9.

## 2 OBSERVATIONS

### 2.1 ATCA Observations

Observations of the 21cm HI line were made over a 7x6 degree field using the 375 m configuration of the ATCA. These

<sup>\*</sup> The Australia Telescope Compact Array and Parkes telescopes are part of the Australia Telescope which is funded by the Commonwealth of Australia for operation as a National Facility managed by CSIRO

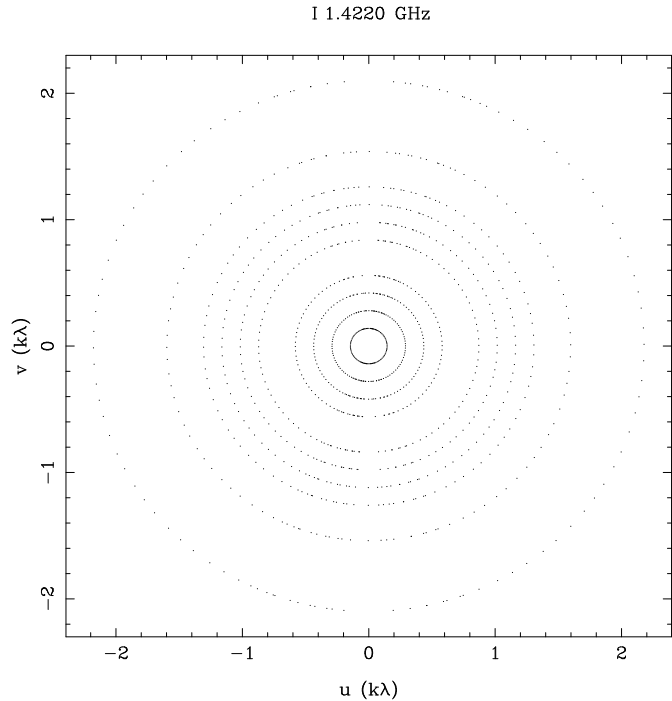


**Figure 1.** UV coverage for pointing #20 of 'block 4', centred at RA 02<sup>h</sup>06<sup>m</sup>07.6<sup>s</sup>, Dec–74°39'55.1''. This is a typical example of the UV coverage for these observations. There are a total of 480 centres over the entire field.

observations were made over three sessions: 1997 April 13, 15-16, 18; 1997 October 9-15; and 2000 January 29-February 2. The 7x6 degree field is broken into 12 'blocks', with each block containing 40 pointings. Each pointing is visited for twenty seconds, approximately once every 15 minutes. The total integrated time for each pointing is thus  $\sim 16$  minutes.

Most of the blocks were observed at this rate over 12 hours for complete UV sampling. Five of the blocks were not observed for a full 12 hours, although these are incomplete by only 6 per cent, and it is not considered that significant artifacts exist in the final image data. The UV coverage of the central pointing (pointing #20) for block 4 is shown in Fig.1 as an example of the UV sampling for these observations.

The ATCA observations were made using a 4 MHz bandwidth, with 1024 channels at a central frequency of 1.420 GHz, resulting in a channel spacing of  $0.83 \text{ km s}^{-1}$  before Hanning smoothing.

The calibrator PKS B1934-638 was observed as a flux standard. This is assumed to have 14.9 Jy at 1.42 GHz. Where this could not be observed, PKS B0407-658 was observed instead, this is assumed to have 14.4 Jy at 1.42 GHz. PKS B0252-712 was used for phase calibration where possible, otherwise PKS B0454-810 was used. At 1.42 GHz, PKS B0252-712 is scaled to 5.7 Jy, and PKS B0454-810 is scaled to 1.10 Jy.

The primary flux calibrator was observed before (and after, where possible) each observing session, none of which lasted for more than twelve hours. The phase calibrators were observed approximately every fifteen minutes.

The MIRIAD data reduction suite was exclusively used

for processing and reduction of the ATCA visibility data, and for the construction of the final image data cube. The data were Hanning smoothed using the MIRIAD task ATLOD to a channel spacing of  $\sim 1.63$  km s $^{-1}$ . Standard editing and calibration methods were followed to create an image datacube (eg. Stanimirović, 1999): INVERT was used to linearly create a dirty image mosaic from the visibilities, using a robustness parameter of zero to down-weight the longer baselines, this has a final sensitivity of 0.9 K. Deconvolution was done with MOSMEM, which uses a maximum entropy algorithm to deconvolve the dirty image cube. RESTOR was used to add back in the residuals and convolve the data with a 98'' gaussian function.

## 2.2 Parkes Observations

Observations were made using the Multibeam receiver on the 64m Parkes telescope, during 1999 November 2nd-8th. Only the seven inner receivers of the Multibeam array were used, with each beam having a FWHM width of 14.1''. Forty-eight overlapping scans were made in Declination, using the on-the-fly mapping mode at 1°/min in Declination. The scans were centred on RA 02<sup>h</sup>00<sup>m</sup>, Dec -72°20', and extended 8° in Declination and in RA, large enough to fully encompass the area observed with the ATCA. The scans were interleaved with a spacing of 1.11°, with a continuously rotating receiver so as to maintain a relative angle of the scan tracks of 19.1° to the sky. The final spacing between adjacent beam tracks was  $\sim 6.7'$ . An 8 MHz bandwidth was used, with 2048 channels and centred on 1.42 GHz. This gave a channel spacing of 0.83 km s $^{-1}$ . These observations were frequency-switched with a frequency throw of +3.5MHz, equivalent to  $\sim 896$  channels and  $\sim 739.5$  km s $^{-1}$ .

The data were reduced and bandpass calibrated using the AIPS ++ online data reduction system LIVEDATA. LIVEDAT was also used to apply velocity corrections. The cube was gridded using the SDFITS2CUBE algorithm (SLAP package, Staveley-Smith, L. Priv comm.), resulting in a beam FWHM of 15.7''. The final Parkes data cube encompassed Heliocentric velocities from 100 km s $^{-1}$  to 350 km s $^{-1}$ .

## 2.3 Merging of ATCA and Parkes Data

Stanimirović (1999) concluded that for telescopes where there is significant overlap in the UV plane (i.e.  $D_{\text{singledish}} >>$  shortest baseline), the differences between merging methods, where single dish data is added to interferometric data before, during, or after deconvolution are usually minimal, and as such, a linear, post-deconvolution method was employed here for its simplicity. The ATCA and Parkes data cubes were combined using the MIRIAD task IMMERGE. The Parkes data were first Hanning smoothed to the same velocity resolution as the ATCA data and regredded to the same spatial and velocity dimensions using the MIRIAD task REGRID. IMMERGE scales the Parkes data by comparing the real and imaginary parts of the ATCA and Parkes data in a region in the Fourier plane that is common to both datasets. It then linearly adds the two data sets so the combined amplitude-spatial frequency response curve returns to a gaussian form, with a width equal to that of the ATCA data (MIRIAD manual, Sault, Killeen 1999). For perfectly

calibrated and stable telescopes the scaling factor should be equal to 1, however, data quality varies over time and from telescope to telescope, and this factor is determined more accurately using IMMERGE. A scaling factor of  $\sim 1.15$  for the Multibeam dataset is used during combination of the Parkes data from these observations.

The combined cube is converted to brightness temperature using the relation;  $S = 2k\Omega T_B / \lambda^2$ , where  $\Omega$  is the beam area of the combined cube ( $=\Omega_{\text{ATCA}}$ ). The combined cube covers a velocity range of 100 km s $^{-1}$  to 350 km s $^{-1}$  with 152 channels. It has a velocity channel spacing of 1.65 km s $^{-1}$  and an RMS of 0.8 K beam $^{-1}$  as measured in line free channels of the cube. This corresponds to a column density of  $1.7 \times 10^{18}$  cm $^2$  for each velocity channel, assuming the mass is optically thin. The final angular resolution is 98''.

Fig.2 shows the integrated intensity maps of the RA-Dec and RA-Velocity projections of the combined ATCA/Parkes data cube, while the Velocity-Declination projection are shown in Fig. 3

The RA-Dec projection of the cube, shown in Fig.2a, reveals the Magellanic Bridge is dominated by filaments, loops and arcs, down to the smallest scale of 98''. This map shows a region of relatively high H<sub>I</sub> column density running East-West, where the H<sub>I</sub> column density is higher than the background diffuse component by a factor of  $\sim 20$ . The highest column density in this east-west strip is  $5.5 \times 10^{21}$  cm $^{-2}$  at RA 1<sup>h</sup>23<sup>m</sup>59<sup>s</sup>, Dec -73°07'43'', although this point is inside the SMC. Outside of the SMC eastern wing, the highest column density is  $\sim 2.8 \times 10^{21}$  cm $^{-2}$  at RA 01<sup>h</sup>58<sup>m</sup>09<sup>s</sup>, Dec -74°17'28''.

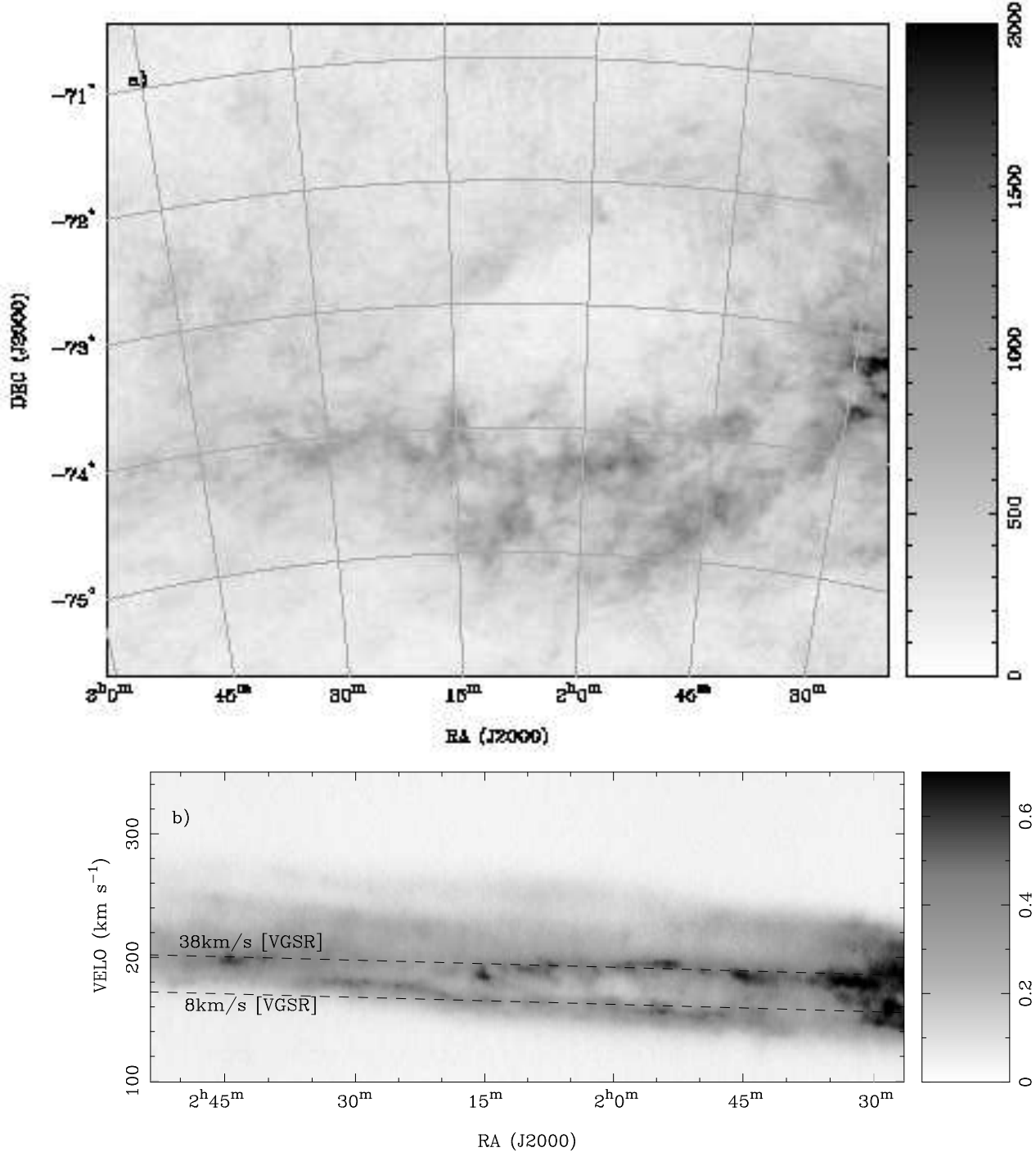
## 2.4 The complete H<sub>I</sub> cube.

Perhaps the most striking feature of these maps is a large loop shaped filament, centred on RA  $\sim 02^{\text{h}}09^{\text{m}}59^{\text{s}}$ , Dec  $-73^{\circ}21'56''$ . The column density of the loop varies between  $\sim 0.5-1 \times 10^{21}$  cm $^{-2}$ , while the mean column density of the interior of the loop is  $\sim 0.2 \times 10^{21}$  cm $^{-2}$ . The radius of the loop is  $\sim 1^{\circ}$ , corresponding to a projected diameter of  $\sim 1.1$  kpc, assuming that its distance is the same as the adjacent SMC of 60 kpc (e.g. Stanimirović 1999).

Lines of constant velocity (38 km s $^{-1}$  and 8 km s $^{-1}$ ) in the galactic rest frame are included on the RA-Velocity map of Fig.2b. The conversion from Heliocentric to Galactic rest-frames is made with the relation:  $V_{\text{GSR}} = V_{\text{Hel}} + 232 \sin(l) \cos(b) + 9 \cos(l) \cos(b) + 7 \sin(b)$  (eg. Paturel et al, 1997).

The velocity projections of the cube are shown in Figs.2b and 3. These figures reveal more striking structure, in particular, an apparent velocity bimodality can be seen in the RA-Vel plot of Fig.2b, and to a lesser extent in Fig.3. Closer to the SMC, the velocity profile appears to be trimodal, and this will be discussed later. The separation of the velocity peaks is  $\sim 30-40$  km s $^{-1}$  and appears to be roughly constant in RA from the SMC up to RA 2<sup>h</sup>17<sup>m</sup>, where it suddenly converges to a single velocity of 180 km s $^{-1}$  [H<sub>elio</sub>]. Fig.3 also reveals interesting velocity structure. The bimodality seen in Fig.2b manifests as two parallel sheets in velocity at  $\sim 150$  km s $^{-1}$  and  $\sim 190$  km s $^{-1}$ . In addition, a large mass, contained between  $\sim -71^{\circ}$  to  $\sim -73^{\circ}30'$ , can be seen to have a significantly higher positive velocity than the bulk of the Bridge gas by  $\sim +40$  km s $^{-1}$ . The large ring-

**Figure 2.** Integrated intensity maps of Right Ascension-Declination and Right Ascension-Velocity projections of combined ATCA-Parkes datacube. Greyscale is linear as shown on the intensity wedge. Units are  $\text{K} \cdot \text{km s}^{-1}$ . A conversion to column density ( $\text{atm/cm}^{-2}$ ) can be made by multiplying the integrated intensity by  $1.8 \times 10^{18}$ . Shown here are a)RA-Dec projection and b)Vel-Dec projection (see Fig.3 for Ra-Vel projection) Velocities are in the Heliocentric rest frame. The upper and lower lines in b) denote velocities of 38 and 8  $\text{km s}^{-1}$  respectively, relative to Galactic centre.

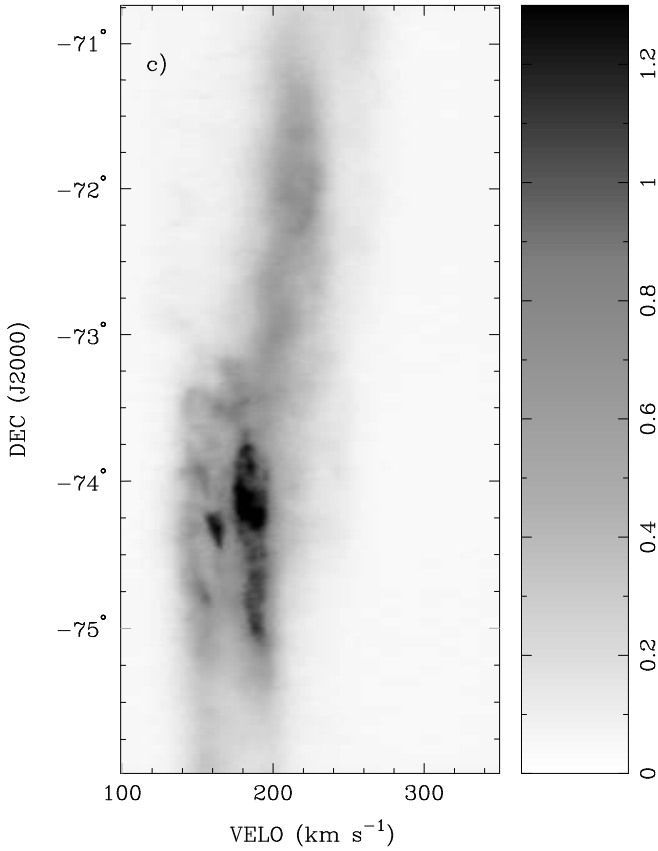


shaped HI void mentioned above is found within this higher velocity mass. Intensity maps of the cube, integrated over groups of five channels (intervals of  $\sim 8 \text{ km s}^{-1}$ ) are shown in Fig.4. The SMC appears in the first few frames on the western side and in general, it can be seen that in the Heliocentric rest frame, the positive velocity of the HI of the

Magellanic Bridge increases with Right Ascension. The large loop filament is particularly obvious in the higher velocity frames centred on  $V_{\text{Hel}} = 194-227 \text{ km s}^{-1}$ .

The mass of the observed region excluding the SMC in the western edge of the observed area (west of  $\sim 1^{\text{h}}35^{\text{m}}$ ), and a  $35''$  margin around the edge of the image is  $\sim 1.5 \times 10^8$

**Figure 3.** Integrated intensity maps of Velocity-Decentraion projection of combined ATCA-Parkes datacube, units and scaling are as for Fig.2



$M_{\odot}$ . However, Fig 2b shows that the central region contains the most mass, and we will see later that the the expanding shell population appears to be more prevalent in this area. If we examine only the central higher-column density region, bounded by  $-75.5^{\circ}$  to  $-73.5^{\circ}$  and  $1^{\text{h}}34'$  to  $2^{\text{h}}46'$  (corresponding to a height of  $\sim 2.1$  kpc, and a length of  $\sim 5$  kpc, see Fig.2a), we find an enclosed mass of approximately  $7.4 \times 10^7 M_{\odot}$  with a surface mass distribution of  $\sim 7 M_{\odot} \text{ pc}^{-2}$ . There are two reasonable approaches to calculate the density of this region:

1. We can assume that the mass of this region is contained within a cylinder of radius  $2.1 \text{ kpc}/2 = 1.1 \text{ kpc}$  and height 5 kpc, then the approximate volume density is  $n_{\text{o}} \sim 0.2 \text{ cm}^{-3}$ .

2. Demers & Battinelli (1998) inferred a depth of the Bridge of  $\sim 5$  kpc by measuring a difference in distance modulus of two adjacent (separated by  $\sim 7'$ ) O associations. If the high density region of the Bridge is modelled as a slab, with a width of 5 kpc, a length of  $\sim 5$  kpc and a thickness of  $\sim 2.1$  kpc, the number density of HI is  $\sim 0.06 \text{ cm}^{-3}$ .

These figures are derived from the central high-density region and the estimate will represent a maximum value for the observed area. The more tenuous gas north and south of the central region has column densities  $\sim 0.3$ - $0.5$  of the central high density region. As the latter value of  $n = 0.06 \text{ cm}^{-3}$  is derived using real depth measurements, we use this value throughout this study.

### 3 THE SHELL SURVEY

A shell or bubble within a gas cloud can be generated through a variety of mechanisms. Currently, one of the most popular theories involves a young energetic star or cluster, which ionises the surrounding gas into a hot, high pressure region and produces a spherical, high-density shockwave which propagates into the ambient neutral gas (Shu 1992). In addition to ionisation, the young star constantly sheds mass in a stellar wind which impinges on the local gas. The result is a relatively low density sphere, enclosed by a higher density hydrogen shell, the outer edge of which is neutral and moves at supersonic velocities into the ambient gas (McCray & Snow 1979). Supernova events will also deposit energy into the medium (Cox 1972) and alternative mechanisms such as Gamma ray bursts (Efremov, Elmegreen and Hodge, 1998) and HVC-disk collisions (Tenorio-Tagle 1981 and Tenorio-Tagle et al. 1987) may also produce elliptical structures with similar appearance. In general, it is very difficult to determine the process by which a particular shell has been formed. HI column density maps will show embedded expanding shells as a relatively bright ring in spatial co-ordinates, and depending on the expansion velocity of the shell, as an ellipse in position-velocity space.

All projections (RA-Dec, RA-Vel and Vel-Dec) of the ATCA/Parkes composite data cube were examined for expanding shells, using the KARMA applications KSLICE-3D and KPVSlice. The criteria for this survey are based on those defined by Brinks & Bajaja (1986) and Puche et al. (1992).

A ring feature was catalogued as an expanding HI shell if the following criteria were satisfied:

*i* - An expanding shell must be observed as a complete ring, or rough ring shape, within the velocity range occupied by the shell (Criterion *iv*, Puche et al., 1992).

*ii* - Expansion must be observable in both Position-velocity projections across at least three velocity channels, and with a stationary centre throughout the channel range occupied by the shell. This criterion was modified from Criterion *ii*, Puche et al, where the ring integrity is examined only in the RA-Dec projection

*iii* - The rim of the ring has good contrast (i.e. relatively high column density) with respect to the ambient column density of the channel maps (Criterion *iii*, Puche et al., 1992).

Note that the criteria here target rim-brightened expanding HI shells, and attempt to exclude HI holes that do not appear to show expansion in both velocity projections. This differs from the HI holes studied in IC10 by Wilcots & Miller (1998) at a channel spacing of  $\sim 2.9 \text{ km s}^{-1}$ , where although all HI holes were examined for a double peaked velocity profile, none were found. The velocities of the receding and approaching sides of the shell, as well as the shell radius (in arcmin), were measured with the KARMA application KSHELL. The Heliocentric velocity of the shell was calculated as the average of the velocities of the approaching and receding sides of the shell, while the expansion velocity is half the absolute difference in these velocities. It should be pointed out here that in an effort to reduce an element of subjectivity, typically inherent in surveys for HI expanding shells, it was required that the three above criteria be strictly satisfied. The effects of such strictness are appar-

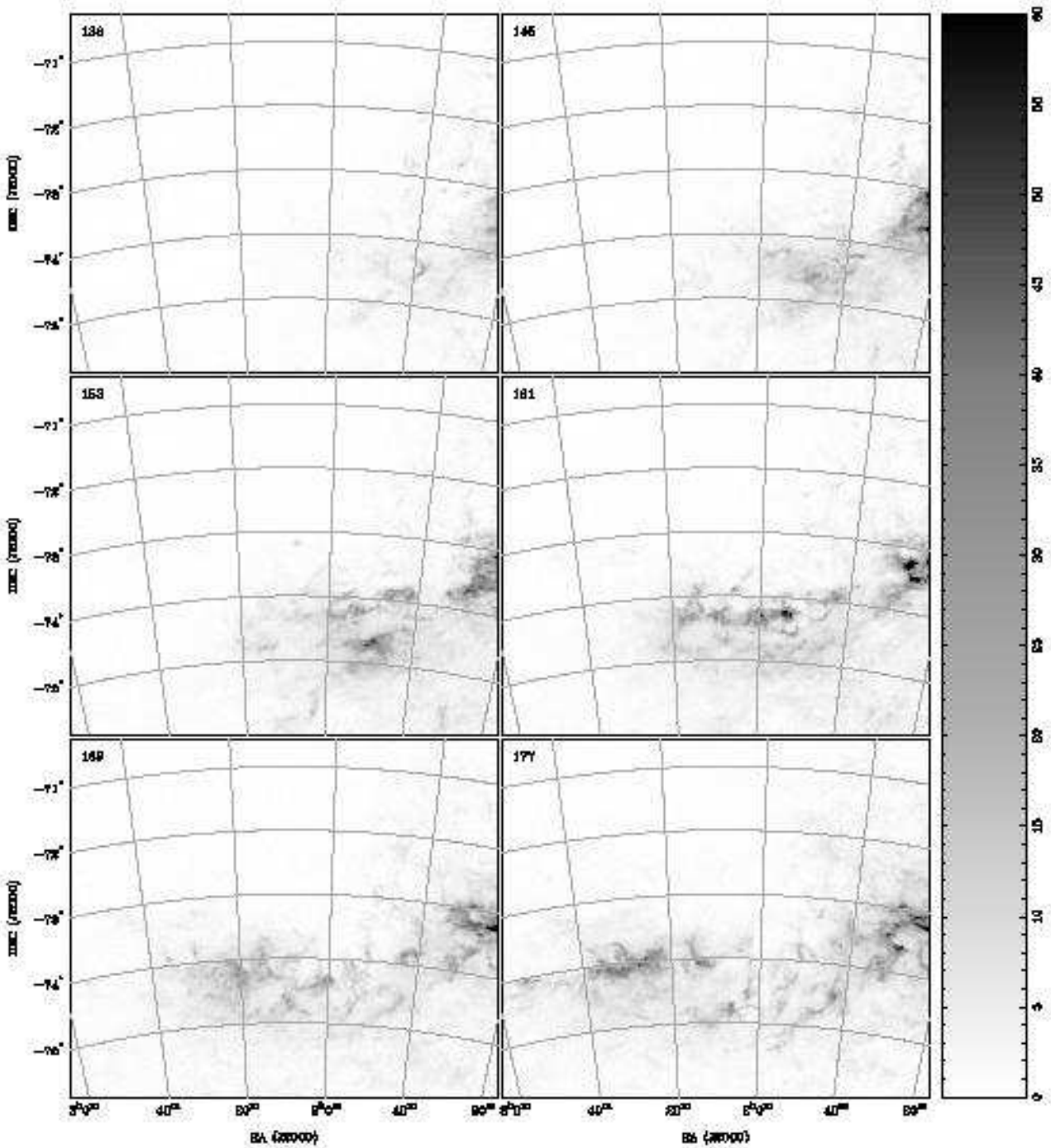


**Figure 4.** Composite ATCA-Parkes HI channel maps over velocity range containing significant signal, of  $135 \text{ km s}^{-1}$  to  $181 \text{ km s}^{-1}$  [Helio]. Each of these panels are integrated over groups of 5 velocity channels ( $\sim 8 \text{ km s}^{-1}$ ). The central velocity is in the top left of each map, and the greyscale is a linear transfer function, with units in K

ent in a statistical examination of the resulting dataset, and these are discussed in Section 6.

Figs 2a and 2b show that the Magellanic Bridge connects smoothly with the SMC, both spatially, and in velocity. These figures also show that the orientation of the Bridge is quite parallel to the lines of constant Declination. By assuming a distance of 60 kpc to the centre of the Small

Magellanic Cloud at  $\text{RA}=1.0^{\text{h}}$  and a distance of 50 kpc to the centre of the LMC at  $\text{RA}=5.33$  hours, we estimate the distance to individual shells within the Magellanic Bridge with a simple linear interpolation between the two Clouds from an empirical relation:  $D(\text{kpc}) = 57.7 - (\text{RA} - 2^{\text{h}}) \times 2.3$ .

To compare shell kinematic ages and luminosities between the Magellanic Bridge, the SMC and other HI systems,

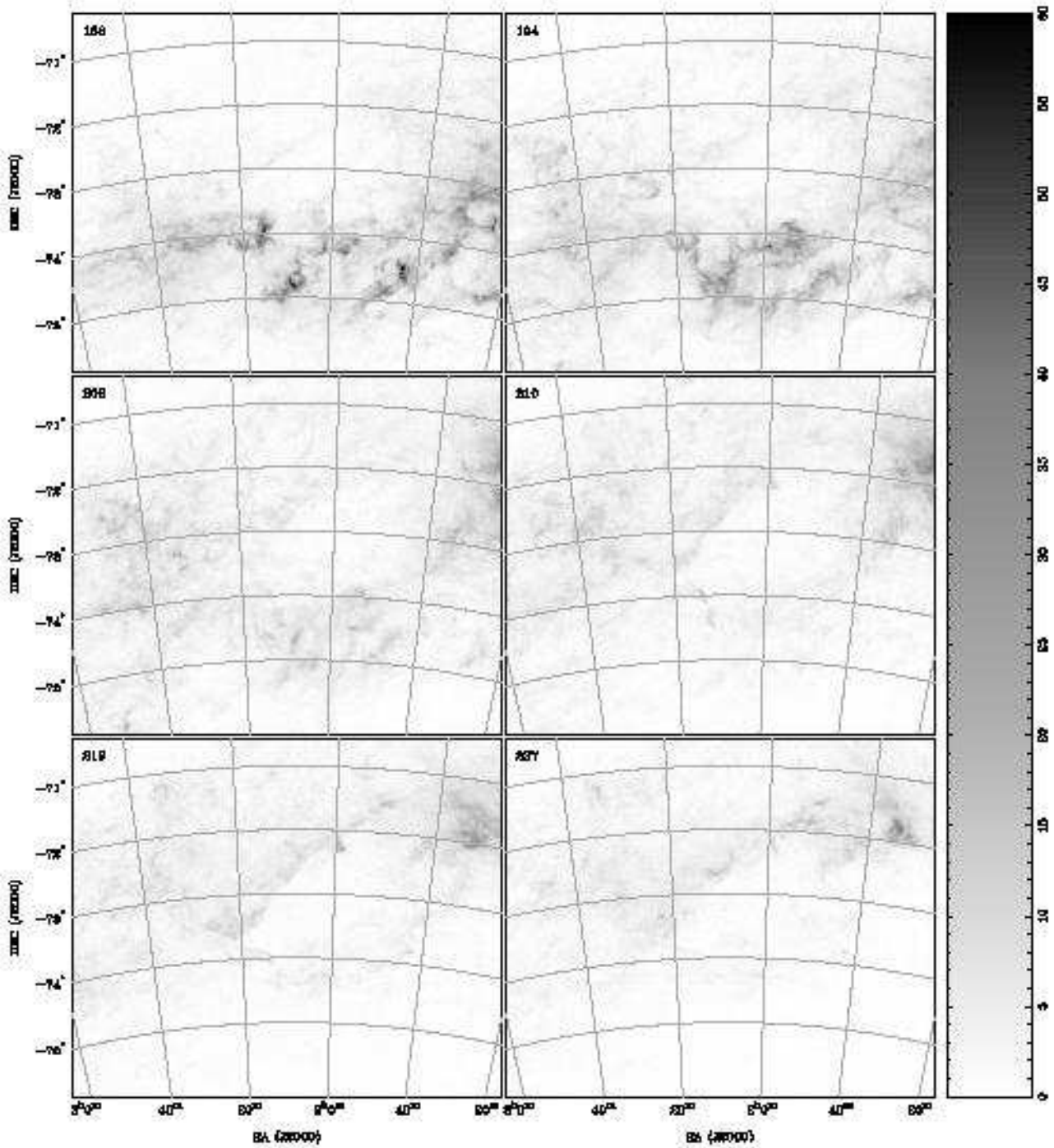


**Figure 4.** Continued, covering the velocity range  $\sim 182$ - $234$   $\text{km s}^{-1}$ . The large  $\sim 1$  kpc loop features prominently in this range.

the following relations, derived by Weaver et al. (1977), are used. The shell kinematic age is found from  $T_s = \frac{3}{5} \left( \frac{R_s}{v_{exp}} \right)$ , with  $R_s$  and  $V_{exp}$  the shell radius in parsecs and shell expansion velocity in  $\text{km s}^{-1}$  respectively. The shell luminosity refers to the power deposited into the local medium

through the action of the stellar wind, and is given by  $L_s = 1.5 \times 10^5 \left( \frac{r}{100\text{pc}} \right)^5 \left( \frac{T}{10^6 \text{yr}} \right)^{-3} \left( \frac{n_\rho}{1 \text{cm}^{-3}} \right) L_\odot$ .

Using a solar luminosity  $\sim 3.9 \times 10^{33}$   $\text{erg sec}^{-1}$ , the relation for shell luminosity is further multiplied by the dynamic age (in seconds) arrive at an estimate of the total shell energy. This formula is derived for a continuous injection of energy into the shell, does not take into account any other

external effects, including magnetic and gravitational forces, and assumes a perfectly homogeneous local gas environment. We use  $n=0.06\text{cm}^{-3}$  as estimated in Section 2.4.

The shell radii, expansion velocities, Heliocentric velocities and dynamic ages are plotted as a function of Right Ascension, and collated for a statistical analysis and comparison with the shells within the SMC.

### 3.1 HI shell survey results and analysis

We have catalogued 163 candidate shells according to the selection criteria of Section 3. The RA, Dec, heliocentric velocity, expansion velocity, radius (in parsec), kinematic age and energy for each shell are shown in Table 1.

The positions of the surveyed shells, as well as the positions of OB associations from a catalogue compiled by Bica & Schmitt (1995), are overlaid on an integrated intensity map of the Magellanic Bridge in Fig.5. A visual inspection of this figure suggests a good spatial correlation between HI column density and expanding shells, and OB associations. This is discussed further in Section 4.

Fig.6 shows the RA-Dec, RA-Vel and Vel-Dec projections for an example shell #51. The expanding volume is clear in the figure.

Magellanic Bridge shell parameters are collated and graphically represented in plots against Right Ascension in Figs. 7a-7d. A comparison of Magellanic Bridge and SMC shell histogram parameters is shown in Table 2 and plotted against Right ascension in Figs 9a-9c. The shell parameters are shown as log histograms in Figs 10a-10d.

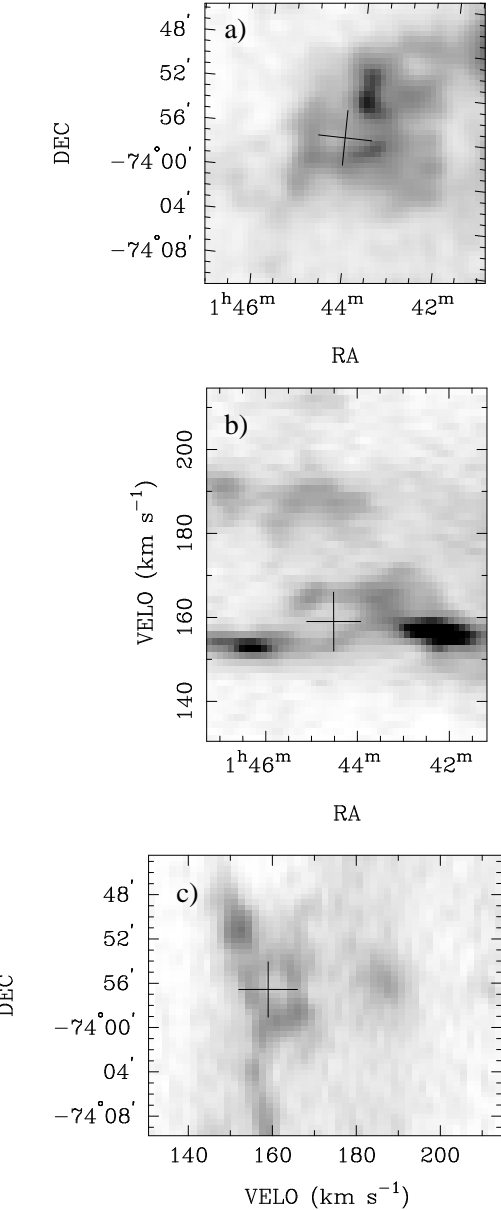
#### 3.1.1 Statistical analysis

Table 2 shows that the average shell radius and expansion velocity of the Magellanic Bridge shell population are smaller than for the SMC population, while the average kinematic age is slightly larger. The dispersions of shell radius and expansion velocity of the Bridge population are also slightly lower than the SMC population, while the dispersion for kinematic age, which is a dependent of both the shell radius and expansion velocity, is slightly larger for the Bridge population. We also see that the mean energy of the shell population is considerably lower in the Magellanic Bridge than for the SMC. To some extent, the disagreement between the mean energy and mean radii here is probably an effect of a different shell selection criteria used for this survey (see also Fig.9). This is discussed in more detail in Section 6.

#### 3.1.2 Right Ascension plots

Figs 7a -7d show the Dynamic age, expansion velocity, shell radius and heliocentric velocity for each of the shells plotted against Right Ascension. A number of observations can be made immediately from these Right Ascension plots:

- There does not appear to be a gradient of shell age with RA, as shown in Fig.7a, although there is a subtle tendency of older shells to be found at higher RA. This is discussed further in Section 6.
- The mean expansion velocity appears to decrease towards the LMC (see also Fig.8). This figure shows also that



**Figure 6.** Three cuts through the combined datacube centred on shell #51. *Top* RA-Declination projection, *Middle* RA-Velocity projection, *Bottom* Velocity-Declination projection. The cross overlay shows the position size and velocity of the shell as it appears in the catalogue of Table1. The greyscale is a linear transfer function, ranging from  $\sim 0$  to  $\sim 50$  Kelvin.

the dispersion of expansion velocity is reduced after  $2^{\text{h}}20^{\text{m}}$ , where the values become less scattered.

- There is no general trend of shell radius with RA, although once again, there appears to a subtle departure into larger radii shells at higher RAs. This is also discussed in Section 6.
- The RA-Vel plot (Fig.7d highlights the smoothly increasing Heliocentric velocity of the HI shells of the Magellanic Bridge towards the LMC, and shows a few shells arranged in apparent loops and filaments.

Fig.8 shows the variation of the mean dynamic age, mean expansion velocity and mean shell radius against RA

**Table 1.** Table of Magellanic Bridge Shell Parameters

Shell Number	Right Ascension (J2000)	Declination (J2000)	Heliocentric Vel. ( km s <sup>-1</sup> )	Exp. Vel. ( km s <sup>-1</sup> )	Radius (')	Radius (pc)	Dynamic Age (Myr)	Energy (log erg)
1	01:21:36.1	-73:29: 3.0	150.3	4.1	3.0	54.3	7.9	47.9
2	01:22:39.7	-73: 5:30.2	172.6	12.1	5.0	90.7	4.5	49.5
3	01:22:59.0	-73:25:30.9	168.2	11.0	3.5	63.1	3.4	49.0
4	01:23: 1.1	-74: 6:23.3	158.5	7.6	3.0	54.7	4.3	48.5
5	01:23: 6.2	-73:30:24.0	189.5	2.1	2.9	53.3	15.0	47.3
6	01:24:24.5	-73:23:24.9	151.8	8.0	3.2	58.3	4.4	48.6
7	01:24:48.5	-74:35:50.9	192.9	3.8	5.9	107.4	17.1	48.7
8	01:24:58.6	-73:11:38.8	147.2	6.0	1.7	30.8	3.1	47.5
9	01:24:59.9	-73:55:55.4	164.0	10.8	5.2	94.3	5.3	49.5
10	01:25:30.5	-72:58:50.8	147.8	8.2	3.2	57.3	4.2	48.6
11	01:25:40.1	-73:32:23.6	173.4	12.4	3.7	66.8	3.2	49.1
12	01:25:40.1	-74: 3: 3.9	167.3	4.9	1.8	31.8	3.9	47.4
13	01:27: 6.6	-73:28:41.7	147.0	5.8	2.1	38.5	4.0	47.8
14	01:27: 8.7	-73:57: 6.7	147.0	5.8	2.7	48.3	5.0	48.1
15	01:27:34.3	-74: 4:34.1	147.8	5.0	1.2	21.1	2.6	46.8
16	01:27:49.0	-73:17: 3.5	175.9	5.0	3.5	62.6	7.6	48.3
17	01:27:54.6	-73: 4:56.4	185.1	3.7	1.8	33.4	5.5	47.2
18	01:28: 3.0	-74: 5:41.3	139.6	3.3	1.6	28.2	5.1	46.9
19	01:28: 8.0	-71:19:46.1	204.7	2.5	0.6	11.2	2.7	45.4
20	01:28:48.4	-73:46:15.5	153.5	5.9	3.2	58.9	6.0	48.3
21	01:29: 8.3	-73: 6:55.5	161.8	15.7	6.9	125.3	4.8	50.2
22	01:29:36.7	-73:41:17.0	165.1	6.8	2.2	40.8	3.6	48.0
23	01:29:38.2	-73: 1:54.7	184.9	5.8	1.7	31.6	3.3	47.5
24	01:29:41.0	-73:17:30.0	175.0	2.5	3.9	71.6	17.4	47.8
25	01:29:50.5	-73: 3:54.9	186.7	5.0	1.7	31.7	3.8	47.4
26	01:29:53.3	-73:56:56.2	169.3	6.6	1.2	22.4	2.0	47.2
27	01:30:14.3	-73:59:26.6	159.5	18.3	5.0	90.1	3.0	49.9
28	01:30:44.4	-73:49:42.0	160.2	2.5	2.5	45.2	11.0	47.2
29	01:30:50.3	-73:42:32.8	171.5	7.6	0.9	16.7	1.3	46.9
30	01:31: 0.8	-73:57:16.1	150.3	5.8	3.8	68.2	7.1	48.5
31	01:31:42.3	-73:46:20.6	157.2	7.7	3.2	58.7	4.6	48.6
32	01:31:43.3	-73:52:25.4	173.4	5.8	3.4	62.5	6.5	48.4
33	01:31:56.5	-73:59:39.0	177.3	4.7	2.7	49.3	6.3	47.9
34	01:32: 7.4	-73:54:43.4	175.4	7.8	2.2	40.5	3.1	48.1
35	01:32: 9.9	-73:30:28.4	186.1	4.0	1.2	20.9	3.1	46.6
36	01:32:28.8	-74: 5: 3.7	156.9	5.8	1.9	33.8	3.5	47.6
37	01:32:31.0	-74: 4: 4.6	173.0	8.7	2.5	44.6	3.1	48.3
38	01:32:44.0	-73:10:36.6	178.4	10.7	3.7	67.0	3.8	49.0
39	01:33:22.8	-71:48:40.0	219.2	5.0	3.1	56.3	6.8	48.1
40	01:33:45.4	-73:56:49.3	151.7	5.0	3.9	71.5	8.6	48.5
41	01:34: 0.8	-71:56:16.8	221.2	4.1	2.2	40.3	5.9	47.5
42	01:34: 1.6	-71:45:36.7	217.4	9.4	3.7	67.8	4.3	48.9
43	01:34:35.3	-71:59:16.7	206.5	16.9	4.5	82.1	2.9	49.7
44	01:34:40.5	-72:53:42.3	208.8	4.9	4.5	81.0	9.8	48.6
45	01:35:30.8	-72:56:17.7	194.0	8.2	4.5	82.4	6.0	49.1
46	01:37:28.5	-74:18: 4.7	151.9	10.7	3.7	67.2	3.8	49.0
47	01:41:13.7	-74:17:12.3	149.5	6.6	2.3	42.1	3.8	48.0
48	01:41:34.9	-73:55:11.1	166.0	9.9	4.1	74.4	4.5	49.1
49	01:42:35.9	-73:49:56.2	162.7	3.3	1.5	27.1	4.9	46.8
50	01:43:26.2	-72:50:40.3	141.2	14.8	5.9	106.5	4.3	49.9
51	01:44:13.0	-73:56:33.6	159.4	6.6	2.4	42.6	3.9	48.0
52	01:45:22.9	-74:30: 6.7	146.3	6.7	1.8	32.8	2.9	47.7
53	01:45:42.2	-74:37:44.4	148.6	4.1	2.0	36.0	5.2	47.4
54	01:45:53.5	-73:14:36.7	177.5	4.9	3.2	58.7	7.1	48.2

**Table 1.** Table of Magellanic Bridge Shell Parameters

Shell Number	Right Ascension (J2000)	Declination (J2000)	Heliocentric Vel. ( km s <sup>-1</sup> )	Exp. Vel. ( km s <sup>-1</sup> )	Radius (')	Radius (pc)	Dynamic Age (Myr)	Energy (log erg)
55	01:46:10.2	-74:28:26.5	181.6	5.8	5.5	99.7	10.4	49.0
56	01:46:13.9	-74:38:14.5	148.6	4.1	1.7	30.9	4.5	47.2
57	01:46:15.5	-74:35:28.3	172.6	21.4	6.7	121.6	3.4	50.4
58	01:47:50.3	-74: 9: 4.4	153.0	4.8	2.8	51.1	6.4	48.0
59	01:48:21.7	-74:37:16.0	193.2	2.5	2.0	36.2	8.8	47.0
60	01:48:50.7	-74:43:32.9	156.9	2.5	1.8	33.0	8.0	46.8
61	01:49:41.1	-74:21:14.6	157.7	11.5	3.6	65.7	3.4	49.1
62	01:50:47.3	-74:22: 6.0	140.4	2.5	1.3	23.4	5.7	46.4
63	01:50:53.0	-74:58: 2.2	194.0	5.0	3.5	62.8	7.6	48.3
64	01:51:20.8	-74: 4:17.7	160.2	10.7	7.1	128.1	7.2	49.9
65	01:51:37.8	-71:29:54.2	218.7	3.3	5.0	91.4	16.6	48.4
66	01:52: 1.3	-74: 7:30.4	193.2	2.5	0.7	12.5	3.0	45.6
67	01:52:39.9	-74:28:39.3	166.7	9.2	3.6	65.4	4.3	48.9
68	01:52:55.7	-74:25:55.6	155.2	2.5	0.9	16.7	4.0	45.9
69	01:53: 7.1	-73:59:49.6	177.5	16.5	5.4	98.4	3.6	49.9
70	01:53:42.2	-71:56:22.3	221.2	7.4	3.8	68.9	5.6	48.7
71	01:53:54.5	-73:55:32.6	174.5	16.4	11.2	203.9	7.5	50.8
72	01:53:56.6	-71:54:25.2	227.8	4.1	3.5	63.9	9.3	48.1
73	01:54: 7.5	-74:39:59.6	173.2	14.7	5.7	104.0	4.2	49.9
74	01:54:58.2	-74: 6:18.6	176.7	7.4	3.5	63.2	5.1	48.6
75	01:55: 3.3	-74:18:18.2	151.1	3.3	5.6	100.7	18.3	48.5
76	01:55:14.3	-74: 4:22.8	197.3	3.3	2.2	40.1	7.3	47.3
77	01:55:26.0	-71:55:51.5	231.1	2.5	1.0	18.1	4.4	46.0
78	01:55:26.6	-74: 7:25.4	181.6	2.5	1.4	26.2	6.4	46.5
79	01:55:52.4	-74:26:29.3	165.1	14.0	3.6	66.1	2.8	49.2
80	01:56:25.1	-74: 7:38.5	154.4	8.2	2.8	50.5	3.7	48.4
81	01:56:35.2	-74:24:37.4	157.8	6.1	4.0	72.2	7.1	48.6
82	01:57:44.1	-74:16:46.9	153.1	4.6	1.7	30.9	4.0	47.3
83	01:58:17.8	-74:15: 0.1	173.4	15.7	3.7	67.7	2.6	49.4
84	01:58:25.4	-74:26:58.8	150.3	7.4	1.8	32.9	2.7	47.8
85	02: 0:42.8	-74:20:22.1	161.8	4.2	1.8	32.8	4.7	47.3
86	02: 3:10.0	-74:47:60.0	154.3	9.7	4.0	72.4	4.5	49.0
87	02: 4:56.9	-74: 9:49.5	169.3	16.5	10.8	195.8	7.1	50.8
88	02: 6:37.1	-74:36:46.6	175.0	12.4	4.2	76.0	3.7	49.3
89	02: 6:40.2	-74: 3:24.4	159.2	5.7	4.5	81.6	8.7	48.7
90	02: 7: 1.1	-74:16:22.8	166.8	7.4	4.9	89.4	7.2	49.1
91	02: 7:14.4	-74:44:13.9	190.6	5.4	4.5	81.1	9.1	48.7
92	02: 7:36.9	-74:52:55.5	178.3	2.5	1.4	25.2	6.1	46.5
93	02: 7:37.6	-74:31:49.5	192.3	3.3	2.2	40.8	7.4	47.4
94	02: 8:22.9	-74:52:42.2	191.5	4.1	1.6	28.3	4.1	47.1
95	02: 9:22.0	-74:24:50.4	159.4	3.3	1.9	34.9	6.3	47.2
96	02: 9:39.6	-74:52:41.1	195.6	8.2	1.7	31.5	2.3	47.8
97	02:10:24.6	-74:45:41.8	168.4	4.1	3.0	54.1	7.9	47.9
98	02:10:43.4	-75: 7:32.4	179.3	5.8	3.1	55.5	5.8	48.2
99	02:10:47.1	-74: 2:21.4	169.3	6.6	6.0	108.7	9.9	49.2
100	02:11:55.9	-74:14:15.8	161.0	5.0	4.5	81.6	9.9	48.6
101	02:11:40.8	-74:46:36.4	178.2	9.5	6.0	108.7	6.8	49.6
102	02:12:41.1	-73:51:45.8	166.8	2.5	0.7	12.9	3.1	45.6
103	02:12:59.9	-74:50:18.2	202.2	9.9	2.8	51.6	3.1	48.6
104	02:13:33.4	-74:19:36.4	180.0	5.8	0.9	16.9	1.8	46.7
105	02:13:38.6	-73:51:40.4	174.2	9.9	9.1	165.6	10.1	50.1
106	02:14:16.4	-74:16: 1.9	171.8	3.7	2.8	51.2	8.2	47.8
107	02:14:19.0	-74:22:30.8	162.5	3.6	1.1	20.2	3.4	46.5
108	02:14:30.1	-74:13:30.9	179.2	6.5	2.7	49.0	4.5	48.2

**Table 1.** Table of Magellanic Bridge Shell Parameters

Shell Number	Right Ascension (J2000)	Declination (J2000)	Heliocentric Vel. ( km s <sup>-1</sup> )	Exp. Vel. ( km s <sup>-1</sup> )	Radius (')	Radius (pc)	Dynamic Age (Myr)	Energy (log erg)
109	02:14:52.2	-73:55:31.4	157.7	4.9	1.4	25.7	3.1	47.1
110	02:14:57.8	-74: 8:59.0	174.8	10.5	3.0	54.2	3.1	48.7
111	02:15:24.1	-74: 2:26.0	176.0	7.9	2.5	45.3	3.4	48.3
112	02:16: 0.2	-74: 1:50.9	174.2	7.1	2.0	36.1	3.1	47.9
113	02:17:31.6	-74: 9: 5.1	179.9	11.6	4.5	81.5	4.2	49.4
114	02:19:44.4	-73:59:40.6	180.0	7.4	6.8	123.8	10.0	49.5
115	02:20: 4.0	-74: 6:35.8	191.8	6.0	3.7	66.2	6.6	48.5
116	02:20:27.5	-74:18:28.7	153.0	4.0	1.5	27.3	4.1	47.0
117	02:20:37.8	-74:41:20.6	163.6	7.4	2.0	36.3	3.0	47.9
118	02:21:49.5	-74:45: 3.8	168.4	2.5	3.0	54.0	13.1	47.5
119	02:21:58.9	-74: 4: 8.2	179.0	6.8	3.5	64.1	5.7	48.6
120	02:22:16.1	-74: 7: 3.6	187.9	2.8	3.0	54.1	11.6	47.6
121	02:22:31.3	-74: 7:58.7	161.8	4.1	1.8	31.8	4.6	47.2
122	02:22:38.2	-74:31:54.4	174.2	4.9	4.0	72.2	8.7	48.5
123	02:23: 0.7	-74: 7:51.3	171.7	4.1	2.2	40.0	5.8	47.5
124	02:23: 9.2	-74:17:17.3	186.5	10.8	7.0	126.4	7.0	49.9
125	02:23:15.9	-74: 0:46.8	186.5	4.2	2.2	40.7	5.8	47.6
126	02:24:22.0	-73: 9:51.4	210.4	12.8	8.0	144.6	6.8	50.2
127	02:24:39.6	-73:13:46.7	210.9	15.6	6.0	108.7	4.2	50.0
128	02:25:21.0	-73:20: 4.4	195.6	4.9	2.3	42.2	5.1	47.8
129	02:25:50.4	-74: 8:59.0	176.2	3.6	2.0	37.1	6.2	47.3
130	02:25:59.9	-73:50:55.5	184.1	6.6	5.8	104.4	9.5	49.2
131	02:27: 8.1	-74: 0: 2.3	189.1	5.6	5.3	95.4	10.2	48.9
132	02:28:20.2	-74: 5: 6.7	177.5	3.3	2.4	42.7	7.8	47.4
133	02:29:27.4	-74:11:41.0	172.6	3.3	4.5	81.0	14.7	48.2
134	02:29:35.0	-73:54:36.6	175.9	3.3	2.9	53.2	9.7	47.7
135	02:30:39.9	-74: 5:40.3	192.9	8.2	4.0	72.5	5.3	48.9
136	02:30:53.6	-73:49: 2.4	180.0	2.5	1.2	22.1	5.4	46.3
137	02:32:46.2	-74: 6:44.8	193.2	3.3	1.5	27.0	4.9	46.8
138	02:33: 8.1	-73:52: 2.2	178.3	2.5	2.4	43.3	10.5	47.2
139	02:33:28.3	-71:14:38.1	218.7	4.9	6.9	125.4	15.3	49.2
140	02:34:20.9	-74:10:31.3	175.0	2.5	3.5	63.9	15.5	47.7
141	02:36:12.9	-73:50:28.3	184.1	3.3	4.0	71.8	13.1	48.1
142	02:36:31.7	-72:44:43.6	217.1	8.2	3.6	66.0	4.8	48.8
143	02:37:14.5	-73: 2:31.0	195.6	3.3	1.1	19.7	3.6	46.4
144	02:37:55.5	-74: 6:38.4	175.0	2.5	1.0	17.4	4.2	46.0
145	02:38:14.9	-73:45:19.3	184.0	6.4	3.0	53.8	5.1	48.3
146	02:40:44.6	-74:10: 1.6	182.4	3.3	3.0	53.7	9.8	47.7
147	02:41:57.7	-72:30: 5.2	204.7	5.8	4.0	73.3	7.6	48.6
148	02:42: 1.7	-74:11:43.9	185.7	6.6	2.5	45.0	4.1	48.1
149	02:42: 6.9	-74:14:11.7	187.3	5.6	2.5	45.4	4.9	48.0
150	02:43:10.9	-74: 3:15.0	194.0	6.6	2.7	49.5	4.5	48.2
151	02:43:22.1	-74: 4:18.7	180.4	2.2	1.2	22.6	6.1	46.2
152	02:43:58.2	-74:17: 2.4	185.7	3.3	1.2	22.5	4.1	46.6
153	02:44:21.8	-73:24:49.1	191.5	4.1	3.3	59.0	8.6	48.0
154	02:44:25.6	-75:12: 3.8	201.9	3.9	2.5	45.3	6.9	47.6
155	02:44:31.8	-73:19:53.9	193.2	4.1	3.5	63.4	9.2	48.1
156	02:46: 1.2	-73:59:27.8	191.5	4.1	1.1	20.0	2.9	46.6
157	02:46: 7.5	-74: 8:29.2	187.4	4.9	2.4	44.0	5.3	47.8
158	02:46:50.2	-73:30:29.9	193.2	4.1	1.3	23.3	3.4	46.8
159	02:47:46.1	-74: 0:12.2	198.1	5.8	2.5	44.6	4.6	48.0
160	02:48:22.5	-75:49:42.1	201.4	4.1	2.4	44.1	6.4	47.7
161	02:50:26.4	-75:52:17.8	200.6	3.3	4.2	75.9	13.8	48.2
162	02:53:55.7	-74: 5:22.7	184.1	3.3	3.9	70.9	12.9	48.1
163	02:54: 3.4	-73:39:47.1	210.2	2.7	2.0	36.3	8.2	47.0

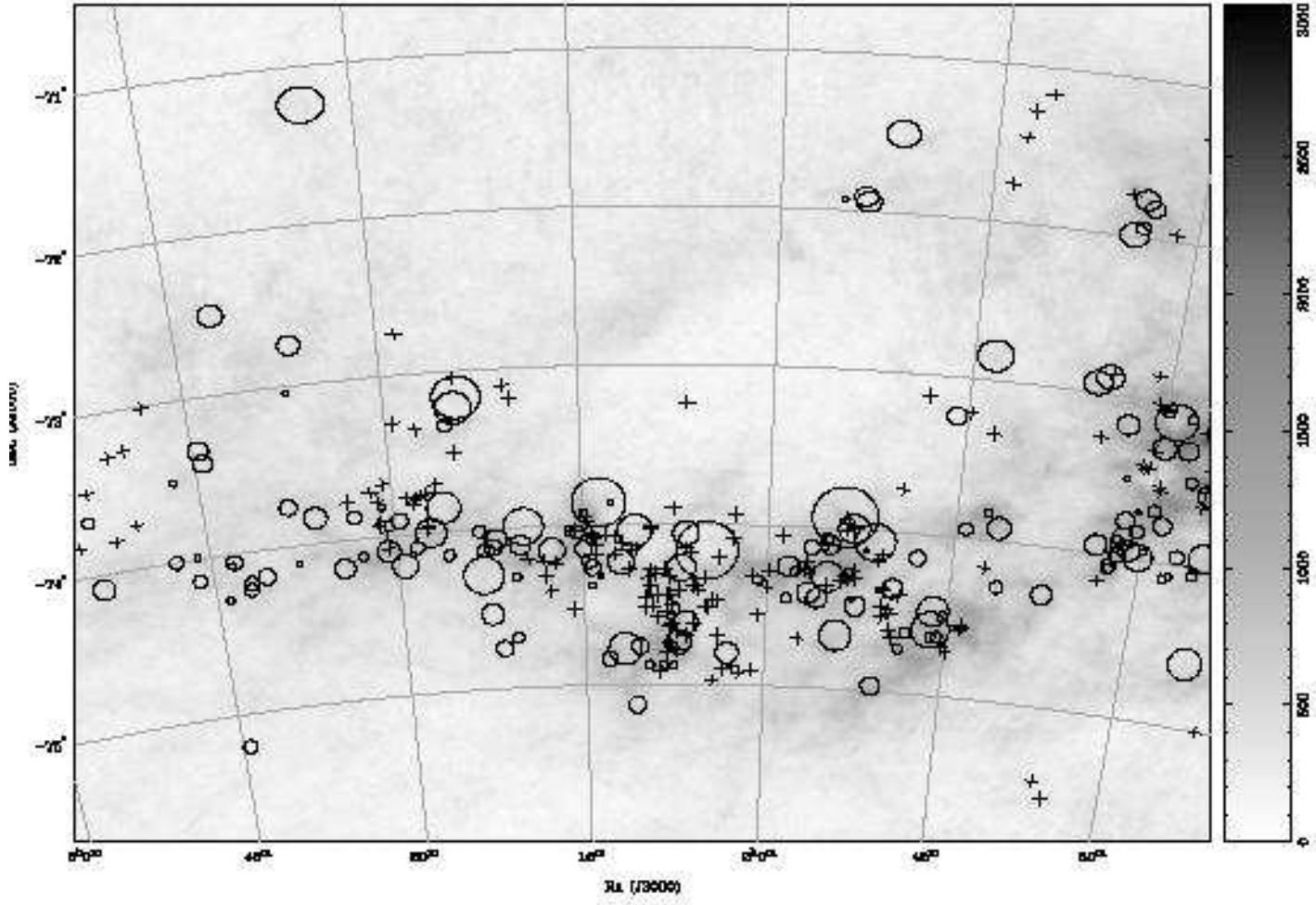


**Figure 5.** HI shells and OB associations within the Western Magellanic Bridge from this survey are overlaid on an integrated intensity HI image. The positions of shells are represented as circles, where the circle radii correspond to shell radii. The shells appear to be mainly confined to regions of higher HI column density. Positions of Young OB associations (crosses) have been taken from a catalogue by Bica & Schmitt (1995). Transfer function is linear with units in K·kms.

	Magellanic Bridge	Small Magellanic Cloud
Mean Shell Radius, ( $R_s$ )	58.6 pc	91.9 pc
$\sigma(R_s)$	33.2 pc	65.5 pc
Mean Expansion Velocity, ( $V_s$ )	6.5 km s <sup>-1</sup> & 10.3 km s <sup>-1</sup>	
$\sigma(V_s)$	3.8 km s <sup>-1</sup> & 6.3 km s <sup>-1</sup>	
Mean Dynamic Age, ( $T_s$ )	6.2 Myr	5.7 Myr
$\sigma(T_s)$	3.4 Myr	2.8 Myr
Mean Energy, ( $L_s$ )	48.1 log(erg)	51.8 log(erg)

**Table 2.** Comparison of properties of Magellanic Bridge Shells (this study) and Small Magellanic Cloud Shells (Staveley-Smith et al. 1997). The mean and standard deviation of each property are given

along the sampled region in the Magellanic Bridge. These plots include parameters of shells found during this survey only, and are averaged in five bins across the observed region. This plot highlights some of the above trends.

The mean expansion velocity decreases with RA, slowly at low RA, then more quickly at higher RA  $>\sim 2^h 12^m$ . We

see that the mean shell radius appears to be increasing with RA, peaking at  $\sim 2^h 24^m$ , before rapidly reducing to low radii. The mean dynamic age is relatively low for regions less than RA  $\sim 2^h 24^m$ , after which we see a dramatic increase by  $\sim 45$  per cent at higher RA. Since dynamic age is proportional to radius, and inversely proportional to expansion velocity,

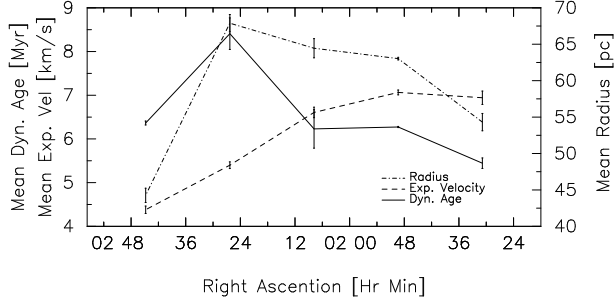


**Figure 8.** Mean Shell dynamic Age (solid line, axis on the left side), Expansion velocity (dash line, left axis), and Shell radius (dot-dash line, right axis), errorbars mark the standard error of the mean.

	Holmberg II	SMC	Bridge
Number of shells	51	509	163
Expansion Velocity, $\alpha_v$	$2.9 \pm 0.6$	$2.8 \pm 0.4$	$2.6 \pm 0.6$
Shell Radius, $\alpha_r$	$2.0 \pm 0.2$	$2.2 \pm 0.3$	$3.6 \pm 0.4$

**Table 3.** Power law of shell radius and expansion velocity ( $\alpha_r$  and  $\alpha_v$ ) for Holmberg II (Puche, 1992), the SMC (Stanimirović, 1999) and the Magellanic Bridge. The Slope in linear space ( $\alpha$ ) is related to the slope in log space ( $\gamma$ ) by  $\alpha = 1 - \gamma$

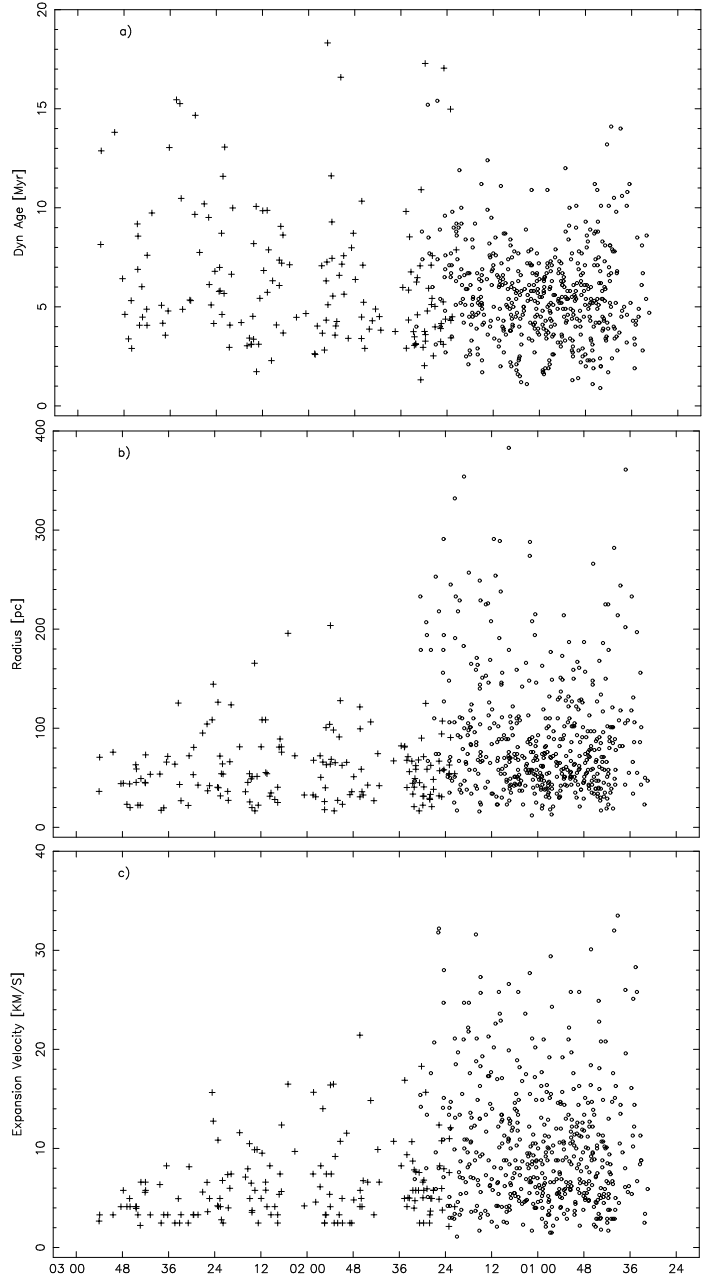
the peak in mean radius at  $\sim 2^h 24^m$ , and the low expansion velocity is manifested as a higher mean dynamic age at this RA. Although the mean radius decreases drastically at higher RA, the expansion velocity has become low enough to allow the dynamic age to remain high. A closer look at Fig.7a shows that, in fact, older shells also exist close to the SMC. These shells are not representative of the region and are washed out in the binning process. The observation that the *mean* dynamic age is larger at higher RA is still true.

Fig. 9a-9c compares the dynamic age, the radii and the expansion velocities of the Magellanic Shells with those of SMC shells (Staveley-Smith et al, 1997). We see from these figures that there is no obvious discontinuity in the mean of the shell kinematic age between the SMC and the Magellanic Bridge. This suggests that there is a continued flow of matter between the two systems. The figures showing the shell radii and expansion velocities (Fig.9c) along the Bridge and SMC reveal a sharp discontinuity corresponding to the position of overlap between the two surveys. These figures highlight differences in shell selection criteria, discussed further in Section 6.

### 3.1.3 Histogram Analysis

Histograms of various properties of the Magellanic Bridge shells are shown in Fig.10. Shell parameters follow a logarithmic distribution (eg. Oey & Clarke, 1997), and the frequency histograms in log space can be fit with linear model. Power law slopes are fitted to each of the parameters: dynamic age, expansion velocity and radius, and are compared with those from the SMC and HoII in Table 3.

These values for each of the slopes vary slightly, depending on the bin size used for each histogram. The tabulated



**Figure 9.** Shell properties of the SMC and Magellanic Bridge as a function of Right Ascension. Top to bottom: a)Dynamic age, b)Shell radius c)Expansion Velocity. Crosses represent shells in the Magellanic Bridge (This survey), while small circles represent data from the SMC shell survey (Staveley-Smith et al, 1997).

figures represent the average  $\alpha$  (where  $\alpha$  is the slope in linear space and is related to the slope in log space  $\gamma$  with  $\alpha = 1 - \gamma$ ), while the errors represent the range of  $\alpha$  while varying the number of bins from 10 to 20.

It can be seen that the power-law fit of the expansion velocity for shells populating the Magellanic Bridge appears to be reasonably consistent with that of the Holmberg II shell population and with the SMC population. Although the slope of the fit to shell radius distribution is considerably steeper, this is most probably due to an deficiency of larger diameter shells (and is discussed in Section 6). When

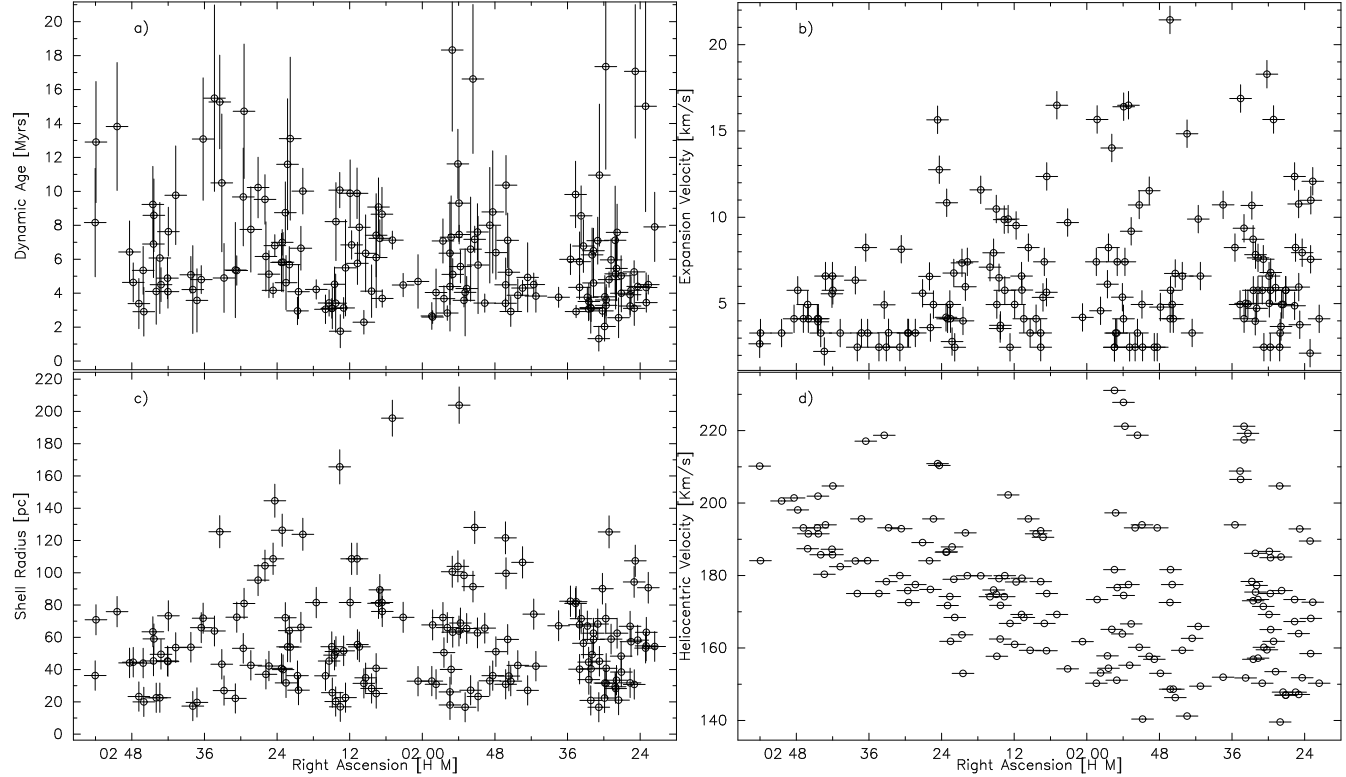


**Figure 7.** Parameters of Magellanic Bridge shells, plotted against RA. a) Dynamic Age, b) Expansion Velocity, c) Shell radius, d) Heliocentric Velocity

comparing these three systems, we should bear in mind that the kinematic conditions of the H<sub>II</sub> galaxy are not necessarily reproduced in the SMC and the Magellanic Bridge. Specifically, H<sub>II</sub> is a disk galaxy and is not obviously tidally perturbed.

#### 4 DISTRIBUTION OF BLUE ASSOCIATIONS

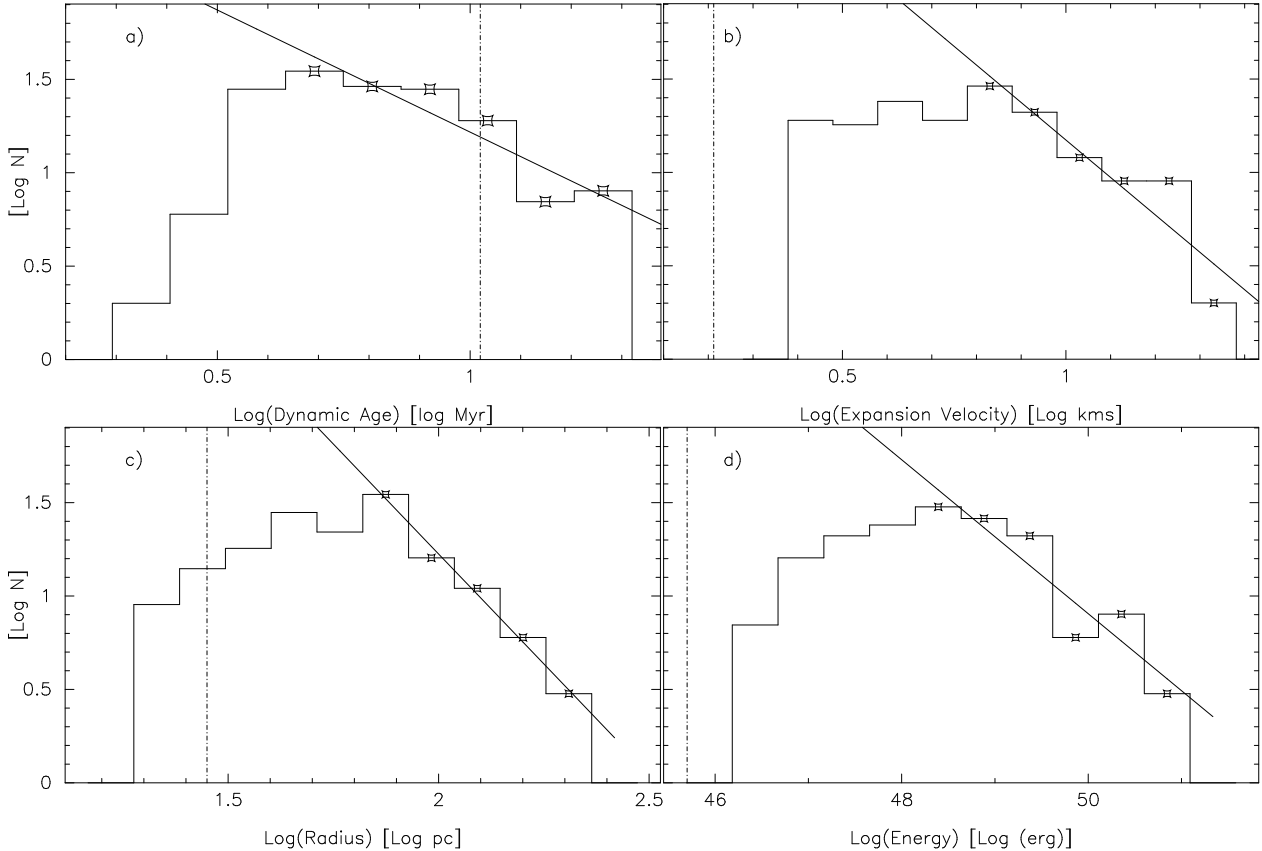
##### 4.1 Spatial correlation with H<sub>I</sub> expanding shells

Fig.5 shows an integrated intensity map of the Magellanic Bridge overlaid with the positions and sizes of H<sub>I</sub> shells, as well as the OB associations found within the Bridge. The latter was initially compiled by Batinelli & Demers (1992) and extended to cover the rest of the Bridge and the SMC by Bica & Schmitt (1995). The limiting magnitude of this association survey is  $V=20.0$ , however, in an attempt to eliminate bright foreground stars, only associations where  $(B-V)>0.0$  were included. A visual examination of Fig.5 shows a general correlation between H<sub>I</sub> column density, the number density of expanding shells, and with the number density of OB associations. The detailed alignment of the associations with shell centres is very poor however, although grouping of young blue clusters about higher H<sub>I</sub> density regions can be seen in many instances, and in particular about the rims of some larger shells and filaments. A more quantitative study of the relative distributions of OB associations and H<sub>I</sub> expanding shells shows that  $\sim 40$  per cent of Magellanic Bridge shells have one or more associations within a distance equal to its radius. If we assume for a moment that associations

are responsible for generating the shell, a displacement over the mean shell radius (60 pc), in over a time interval equal to the mean kinematic age (6 Myr) would require a velocity of only  $\sim 1$  km/s (assuming no inclination of the trajectory of the association to the plane of the sky). However, any motion of the OB association relative to shell would result in the shell having a significantly deformed and non-spherical shape, and would therefore have been excluded from the survey. The poor spatial correlation statistic of OB associations and H<sub>I</sub> expanding shells is contrary to the popular theory of the formation of stellar wind-driven H<sub>I</sub> expanding shells (Weaver et al, 1977). Similarly however, we should also bear in mind that the mean Magellanic Bridge shell age is approximately equivalent to that of an O type star, and any related stellar association may be too faint to have been included in the OB catalogue. A study of the spatial correlation of the SNe and H<sub>I</sub> shell population of the H<sub>II</sub> galaxy has been conducted by Rhode et al. (1999). This study was designed to test the hypothesis of stellar wind and SN explosions acting as the engine for the expansion of a H<sub>I</sub> shells. The conclusions from this analysis were that under the assumption of a normal initial mass function, the OB cluster brightness was such that the H<sub>I</sub> shell distribution was strongly inconsistent with the theory of formation by SNe.

##### 4.2 Properties of nearby H<sub>I</sub>

To quantitatively test the spatial correlation of OB associations and H<sub>I</sub> column density in the Magellanic Bridge, the mean column density of a 90''(3 pixel) box centred on each



**Figure 10.** Number frequency of Magellanic Bridge Shell parameters: *a*) Dynamic age, *b*) Expansion Velocity, *c*) Radius and *d*) Energy. The vertical dot-dash line marks the limits imposed by angular resolution ( $98''$ ) and velocity resolution ( $1.61 \text{ km s}^{-1}$ ). As the distributions of Shell parameters follow a logarithmic law, we are able to determine a characteristic slope in  $\log(N)$ -log space.

of the catalogued OB association positions is presented as a histogram in Fig.11 (black columns). Overlaid on this is a second histogram, representing the entire map itself (white columns). The histogram shows that  $\sim 50$  per cent of the catalogued OB association positions correlate with a mean column density of  $\gtrsim 1.2 \times 10^{21} \text{ cm}^{-2}$ , only 8 per cent correspond to column densities equal to or less than half that density and  $\sim 10$  per cent are associated with regions of column density greater than  $2.4 \times 10^{21} \text{ cm}^{-2}$ . We find that these are similar to results by Demers & Grondin, who found that stellar positions correlate with column densities  $\sim 10^{21} \text{ cm}^{-2}$ , and that very few associations can be found to correlate with low HI column densities.

The different distributions of the two histograms in Fig.11 confirm that the mean intensities around the positions of the associations are a unique subset of the total dataset, and not simply a random sample, although we should bear in mind that by selecting a  $90'' \times 90''$  box at each association position, we sample less than 2 per cent of the entire map area.

Fig.12 shows the mean column density variation as a function of distance from the centres of each catalogued OB association. A linear fit, with a slope of  $\sim 0.5 \times 10^{18} \text{ cm}^{-2} \text{ pc}^{-1}$ , represents the general decline of column density away from the main HI filaments where OB associations are found. However, there is a significant departure at short radii. This appears to be due to an excess of HI within  $\sim 80 \text{ pc}$

of the OB associations, and is in the opposite sense to that found by Grondin & Demers (1993) for OB stars.

Data used by Grondin & Demers was that obtained from the Parkes telescope by Mathewson & Ford (1984), and has a resolution of  $\sim 14''$  ( $\sim 244 \text{ pc}$ ), whereas the minimum resolution of the dataset used here is  $\sim 98''$  ( $\sim 28.5 \text{ pc}$ ). Fig.12 also shows the mean integrated HI as a function of radius, offset  $5''$  ( $\sim 90 \text{ pc}$ ) south for each OB association. This line shows a peak in HI excess at a distance equivalent to the offset, showing that the excess is real, and is centred on the positions of the OB associations.

## 5 H $\alpha$ REGIONS

A large shell within the Bridge at RA  $02^{\text{h}}07^{\text{m}}14^{\text{s}}$ , Dec  $-74^{\circ}44'14''$  (J2000) was detected in H $\alpha$  and measured by Meaburn (1986), Parker (1998) and by Graham et al. (2001). This H $\alpha$  shell, labelled DEM171 by Meaburn (1986), is found to be closely aligned to an identifiable expanding HI shell at  $\sim$ RA  $02^{\text{h}}08^{\text{m}}8^{\text{s}}$ , Dec  $-74^{\circ}42'46''$ . This shell is found to be a typical example of the Magellanic Bridge shell population, and is parameterised and listed as #91 in Table 1. H $\alpha$  parameters as estimated by Meaburn (1986), Parker (1998) and by Graham (2001) are compared in Table 4. A map of the HI peak brightness temperature, with the positions of

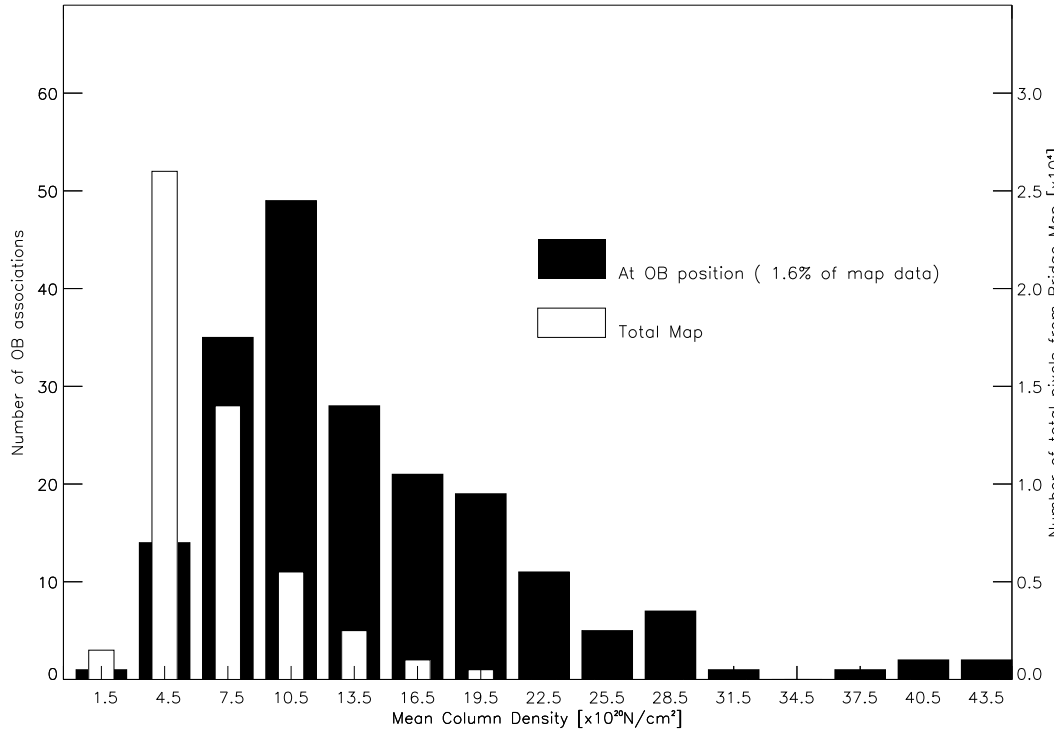


**Figure 11.** Black and left hand axis: Histogram of mean column density within a  $90'' \times 90''$  square centred around each OB association (from catalogue by Bica & Schmitt 1995). White and right hand axis: Histogram of mean column density of entire map. Map is binned into  $90'' \times 90''$  resolution.

	Meaburn (H $\alpha$ )	Parker (H $\alpha$ )	Graham (H $\alpha$ )	Shell 91 (H $\mathrm{i}$ )
Right Ascension (J2000)	02 <sup>h</sup> 07 <sup>m</sup> 50 <sup>s</sup>	02 <sup>h</sup> 07 <sup>m</sup> 56 <sup>s</sup>	02 <sup>h</sup> 07 <sup>m</sup> 14 <sup>s</sup>	02 <sup>h</sup> 07 <sup>m</sup> 14 <sup>s</sup>
Declination (J2000)	-74°44'14"	-74°44'06"	-74°44'14"	-74°44'14"
Radius	3.93'	4.3'	~4'	4.5±0.5'
Apparent age	5 Myr (wind) 8-210 Myr (SN)	—	0.53 Myr	9±2 Myr
Heliocentric Vel	—	—	192.5 km s <sup>-1</sup>	190±2 km s <sup>-1</sup>
Expansion velocity	—	—	37.0 km s <sup>-1</sup>	5±2 km s <sup>-1</sup>
Suggested Source	O star stellar wind, SN	PN, SNR, WR shell	WR	—

**Table 4.** Comparison of parameters of the H $\mathrm{i}$ H $\alpha$  Shell DEM171 (H $\mathrm{i}$  shell#91) as observed in H $\mathrm{i}$  and H $\alpha$  (Meaburn 1986, Parker 1998, Graham 2001), and in H $\mathrm{i}$  (this paper)

the H $\alpha$  shell as measured by Meaburn, and the H $\mathrm{i}$  shell #91 (this paper), is shown in Fig.13.

The ionising mechanism of this H $\mathrm{i}$ /H $\alpha$  shell is still unknown. Meaburn (1986) suggests a single O star is responsible for the illumination of the H $\alpha$  shell. Parker has commented that UV source FAUST 392 corresponds closely to the centre of the shell, is probably a low surface brightness Planetary nebula (PN) or even a supernova remnant, although the low energy derived in the present study does not suggest a typical supernova as the mechanism for this shell. Graham et al. (2001) have located a Wolf-Rayet (WR) candidate within the shell rim, and suggest that this object may be responsible for causing the expansion of the shell. A

number of OB associations are distributed around the high density H $\mathrm{i}$  rim of this region (Bica & Schmitt 1995), and at present, this is the only H $\mathrm{i}$  shell within the Magellanic Bridge that can be unmistakably attributed to a stellar origin.

Table 4 shows that the age and radius determined here for shell# 91 as derived from the H $\mathrm{i}$  data is in general agreement with these parameters determined from H $\alpha$  data by Meaburn (1986), although there is considerable discrepancy of the expansion velocity, and hence the kinematic age with findings of Graham et al. (2001). Fig.14 shows the velocity slice at Declination  $\sim -74^{\circ}44'34''$ . The two peaks, at Heliocentric velocities of  $\sim 185$  km s<sup>-1</sup>– $\sim 196$  km s<sup>-1</sup> are those

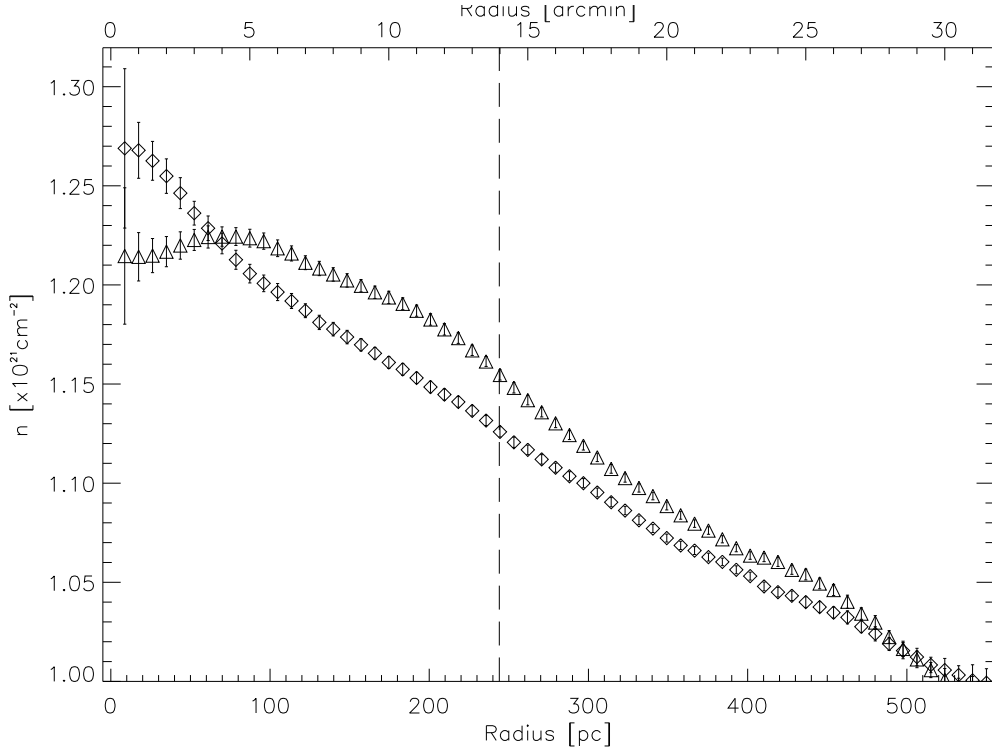


**Figure 12.** Diamonds show mean HI vs radius centred on OB positions, while triangles show mean HI as a function of radius, offset from OB centres by  $\sim 5'$  southward. A positive departure is apparent for radii  $< 80$  pc ( $\sim 5'$ ). The offset highlights the fact that the OB associations are generally associated with a local peak in integrated HI. Vertical dashed line shows limit of spatial resolution from Matthewson & Ford (1984) dataset. Error bars mark one standard error.

corresponding to the approaching and receding sides of the shell. We do not find any HI emission peaks corresponding to those in H $\alpha$  as measured by Graham et al.

In addition, another H $\alpha$  region (region #172) parameterised by Meaburn (1986), is found to correlate well with a similarly shaped high density HI region, as shown in Fig.13.

to fragment after some time. These authors calculate that shells will tend to self-destruct from intrinsic instabilities at radii  $\sim 1$  kpc, which is much larger than the maximum radii of the Magellanic Bridge shell population. There must therefore be additional processes catalysing the fragmentation, or otherwise affecting the integrity of the large-scale H $\alpha$  shells within this population.

## 6 FACTORS AFFECTING THE SURVEY

This survey has selected a sample of shells that, compared with the HI shell population of the SMC, appears to be relatively deficient in large-radius shells (See Fig.9b). This is almost certainly due to a different and tighter selection function. This survey demands a regular and identifiable ring shape in all three projections before such a structure can be accepted as an expanding HI shell. Incomplete, or significantly distorted shells cannot be accurately parameterised, and it is not always clear that such structures are genuine expanding HI shells. Other HI shell surveys have used a more relaxed criteria and have permitted partially incomplete ring shapes to be classified as an expanding shell. Given that this survey is sensitive to the same range of scales of the SMC surveys made by Staveley-Smith et al. (1997) and Stanimirović et al. (1999), this then leads to question the apparent tendency for large shells to be more susceptible to fragmentation and distortion. McCray & Kafatos (1987), Ehlerova et al. (1997) and others have determined that for thin walled expanding shells, instabilities will cause the shell

### 6.1 Deformation by secondary starformation

Star formation occurring within the compressed gas comprising the shell wall may be responsible for deformation of the shell shape. Mass and energy loss from a star forming within the compressed gas of an existing shell may blow open a secondary wind shell in the primary shell wall, leading to deformation of the primary shell, and ultimately, a departure from the signature shell shape. A shell expanding into a low ambient density region will not accumulate a high density rim as quickly as one embedded in a higher density. As star formation usually occurs only after a threshold column density is reached, we might not expect shells that are expanding into a low ambient density medium to be as readily disturbed by secondary star formation. Secondary star formation within the shell wall has been observed in the SMC (Stanimirović, 1999), while small HI shells clustered within the wall of a larger HI shell have also been observed in the LMC (Kim et al. 1999).

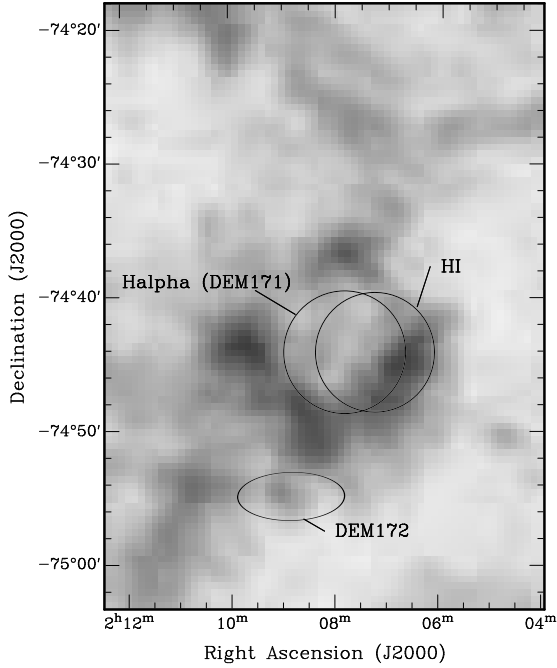


**Figure 13.** HI (shell #91) and numbered H $\alpha$  ‘nebulous’ regions (from Meaburn 1986), overlaid on magnified Ra-Dec peak pixel map. The HI shell is shown to be closely aligned with the H $\alpha$  shell (labelled H $\alpha$ ). The feature to the south, labelled #172, shows the position of one of the H $\alpha$  ‘nebulous regions’ corresponding to a small local HI peak intensity maximum. The reason for the HI and H $\alpha$  shells offset can be seen in Fig.14, where the actual expanding shell appears to have a higher positive central velocity than the ring, and is at a slightly different RA. The figure has a linear transfer greyscale ranging from  $\sim 8$  to  $73 \sim$  Kelvin

## 6.2 Deformation from density stratification

Shell-like features, such as blow-outs, or chimneys, that were not included in this catalogue, were found occasionally throughout the cube. A blow-out, or a tunnel can develop by an expanding shell forming close to a region of much lower relative density. The expanding gas can blow through the boundary separating the two densities, such as through the wall of a gas cloud, and into the low density region. Such structures can also form through the merging of two expanding shells, and have been observed in the Galaxy (eg McClure-Griffiths et al, 2000), as well as other galaxies (eg. Ott et al., 2001). Under these conditions, the calculation of the dynamic age, which is based on an assumption of constant and homogeneous ambient gas density, is incorrect. A study of these shell-like structures will be included in a future project.

## 6.3 Size limitations

Any constraints on shell radii imposed by the extent of the gas in the Magellanic Bridge are not considered to be significant: the height of the high HI density region in the Bridge, in Declination, is almost four times the diameter of the largest shell found from this survey, although it is of the same order of the diameter of the largest supershell in the SMC (Stanimirović, 1999). The largest shell radius

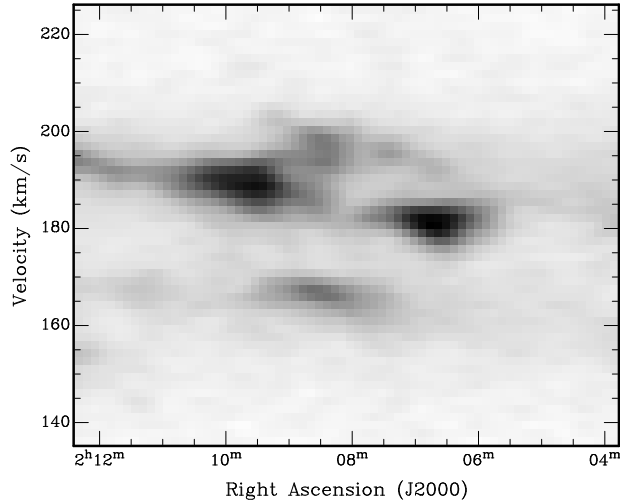


**Figure 14.** RA-Velocity slice at Dec= $\sim -74^\circ 44' 34''$ , centred on DEM171/Hi shell #91. The temperature range is 70 K to  $-0.4$ K, with a linear transfer function. This shows the receding and approaching sides of the expanding shell at  $\sim 185$  km s $^{-1}$  and  $\sim 196$  km s $^{-1}$ . We see here that the actual centre of the shell appears to be shifted slightly to lower RA, and does not correspond to the centre of the HI ring in the RA-Dec projection from Fig.13

found during this survey was  $11.7'$ , equivalent to  $\sim 204$  pc, and the radius of the largest supershell found in the SMC was  $\sim 910$  pc.

## 6.4 Tidal stretching

Given the mechanism of formation of the Bridge, one possible mechanism of deformation is tidal stretching. However, of the shells surveyed, there does not appear to be any significant tendency for elongation or stretching along the SMC-LMC direction, implying that tidal shearing of the shells is not a significant cause of distortion over the time scales considered here.

## 6.5 Change of environment in Magellanic Bridge

Vishniac (1983) has suggested that local inhomogeneities in the ambient HI gas may cause the shell to distort from perfect spherical symmetry and we note that Fig.2 shows the HI has a complex and turbulent structure down to  $98''$  ( $\sim 29$  pc). The chaotic nature of the gas comprising the Magellanic Bridge may be responsible for premature fragmentation of the HI shells. Shells fragmented in this way do not satisfy criteria *i* and are not included in this catalogue. We notice that this survey has uncovered a region within the Magellanic Bridge containing a slight excess of older shells Fig.8). These shells have significantly slower expansion velocity, and although they also have a slightly smaller radius, the net result is a mean dynamical age which is a factor of two or so

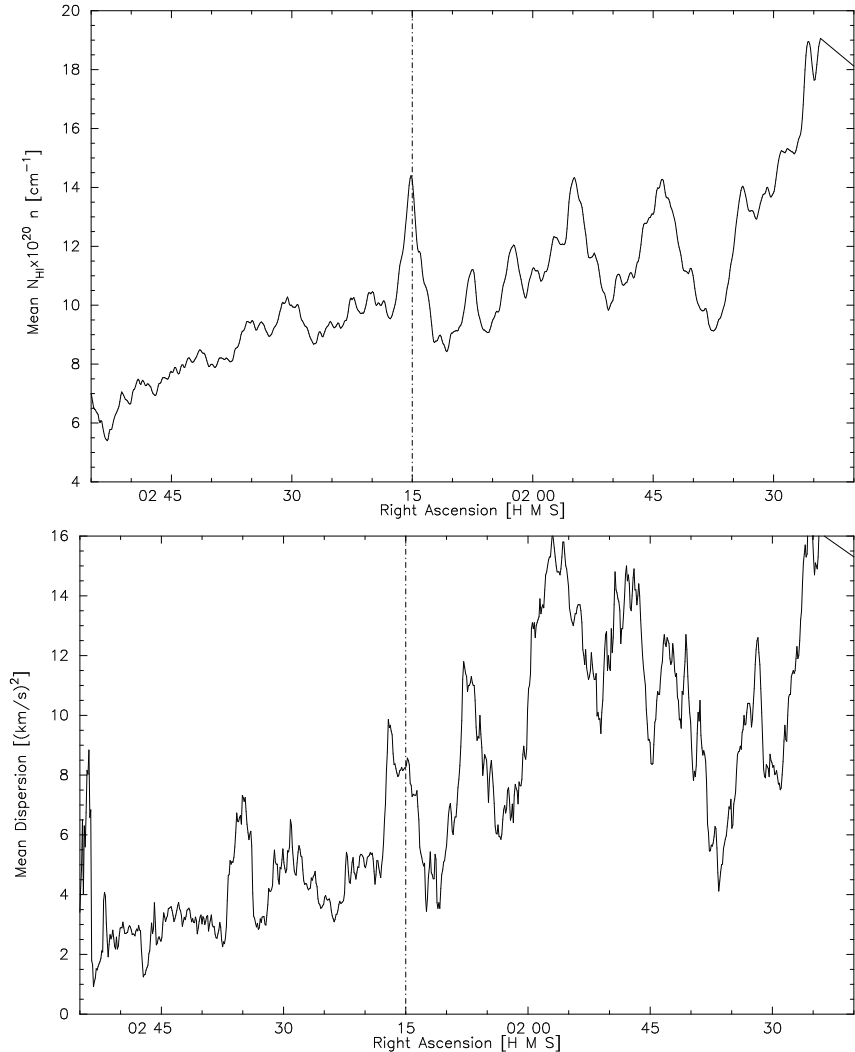


**Figure 15.** The variation of HI integrated intensity (a) (top) and HI velocity dispersion (b) (bottom) with Right Ascension. The data is averaged over the high HI column density region across a selected area of Fig. 2 (approx  $-73^{\circ}40'$  to  $-74^{\circ}40'$ ). These plots suggest sudden change of the properties of HI at Right Ascensions higher than  $\sim 2^{\text{h}}15^{\text{m}}$ .

greater than the rest of the Magellanic Bridge population. The transition of these two regions appears to be at around RA  $2^{\text{h}}15^{\text{m}}$ , with the region containing the older shells lying to the east of this.

The average integrated HI, and HI velocity dispersion for the central region containing the higher HI column density are plotted in Figs 15a and 15b. It can be seen that the fluctuation of the mean column density is relatively low at RA higher than  $2^{\text{h}}15^{\text{m}}$ . Similarly, the velocity dispersion becomes somewhat lower above this RA, although there are still some larger scale variations present, as well as a decreasing gradient with RA. In general however, the velocity dispersion and HI column density are smaller and with less variation above  $2^{\text{h}}15^{\text{m}}$ , suggesting that this region is less dynamic than the western part. A reference to Fig. 2a shows that the large loop mentioned in section 2.4 re-joins the Bridge at approximately this right Ascension. Also, the velocity bimodality in Fig. 2b appears to terminate at this same RA. We suggest that the younger HI expanding shells west of  $2^{\text{h}}15^{\text{m}}$  are more quickly ruptured from the relatively

higher turbulence, and possibly from secondary star formation, while those populating the eastern side remain intact for a longer time, possibly because of the more quiescent nature of the ambient gas. It is unclear at this point what relationship the large loop might have with the change of the HI environment.

## 7 DISCUSSION OF THE STELLAR WIND MODEL.

### 7.1 Energy deposition

The associations catalogued by Batinelli & Demers (1992), which were later included in the catalogue by Bica et al. (1995), constitute many poorly populated (mean  $N \sim 8$ ) associations and clusters. Bica E. (priv. communication) mentions that the associations and clusters become more populated towards the SMC, and that a few of the associations may be composed of later type stars, although the majority are of O-B type. We can see that the shells so far uncovered

are of very low energy. Given that the mean shell energy is rather small when compared with the standard approximation of the energy for a single O5 type star ( $\sim 10^{51}$  erg Lozinskaya, 1992), poorly populated associations, comprising low-mass, later type stars, might be capable of producing low energy structures and may be responsible in some of these cases found in the Bridge. It is curious however, that we do not observe a larger fraction of expanding shells centred about many of these observable associations and clusters, and that the regions surrounding the associations are not depleted in H<sub>I</sub>. The lack of spatial correlation of H<sub>I</sub> shells and an obvious energetic source has been noted before however (e.g. Rhode et al. 1999), and alternative scenarios to the stellar wind engine are discussed in Section 8.

A total of 198 associations and clusters are found within the observed Bridge region where 163 shells are found. The SMC survey constitutes  $\sim 500$  shells, and includes 987 associations and clusters from the same catalogue. We find that we have almost one shell per association or cluster in the Bridge, whereas we have almost two associations or clusters for each shell within the SMC. This could reflect different formation and destruction mechanisms in the two regions. For example, the less turbulent nature of the environment of the Bridge may allow shells to develop for a longer time.

The relatively higher shell population in both cases also calls into question the idea of stellar wind-driven expanding shells, although given a similar kinematic age of shells in the Bridge and the SMC, the relatively higher ratio of shells per association in the Bridge might indicate a relatively less turbulent environment in this region (following the discussion from above).

We find that the mean energy of Bridge H<sub>I</sub> shells is a relatively small value of  $\sim 1.9 \times 10^{49}$  ergs, and a total energy of  $\sim 3.2 \times 10^{51}$  erg. Table 1 shows that only six of the 163 shells have an energy greater than  $10^{50}$  ergs, and none are greater than  $10^{51}$  ergs (for an ambient density of  $\sim 0.06 \text{ cm}^{-3}$ ).

The total H<sub>I</sub> mass of the observed Magellanic Bridge region was calculated in Section 2.4 to be  $1.5 \times 10^8 M_{\odot}$ , giving a shell power per H<sub>I</sub> mass of  $2.1 \times 10^{43}$  ergs/ $M_{\odot}$ . Using a mass of  $3.8 \times 10^8 M_{\odot}$  for the SMC, and a total shell energy of  $\sim 6.7 \times 10^{54}$  erg (Staveley-Smith et al. 1997 and Stanimirović et al. 1999), we calculate a power per H<sub>I</sub> mass of  $1.8 \times 10^{46}$  ergs/ $M_{\odot}$  for the SMC. We see that the shells populating the Bridge are significantly less powerful per mass than those of the SMC. We see also that the median SMC shell energy is  $\sim 10^{50.2}$  erg, and that the median Magellanic Bridge shell energy is some orders lower at  $\sim 10^{48}$  erg. However, given the strict shell selection criteria, these relative values should be considered as lower limit only.

## 7.2 The Ages of Bridge shells, and Bridge OB associations

It can be seen that the average dynamic age of  $\sim 6.2$  Myr (Table 2) of the Magellanic Bridge shell population is far younger than the date of the most recent Magellanic Cloud interaction, shown by simulations to be approximately 200 Myr ago (eg Gardiner, Sawa & Fujimoto, 1994). There is also a lack of agreement with ages of OB associations, determined through isochrone fitting by Grondin, Demers & Kunkel (1992) and Battinelli & Demers (1998), to be in the range 10-25 Myr. These values differ with the average shell

dynamic ages calculated here by up to a factor of almost four. A possible source of error in the determination of the dynamic age is suggested by Shull & Saken (1995) who observe that the fraction of Wolf-Rayet stars in an OB association peaks for associations of around  $\sim 5$  Myr old. The extra luminosity input from the WR stars can accelerate the radii and expansion velocity of the stellar wind shell, and result in a mis-estimation of the dynamic age by up to a factor of three. The average dynamic age calculated here is very close to this time of peak Wolf-Rayet population, although even allowing for re-acceleration by WR stars does still not bring the dynamic age to one that is comparable with the association ages estimated by Grondin, Demers & Kunkel (1992) and Demers & Battinelli (1998). It is difficult, therefore, to become convinced that the majority of the spherical expanding H<sub>I</sub> structures in the Magellanic Bridge are powered by stellar winds.

Figs. 9a-c show that, despite the apparent lack of large radius shells in the Magellanic Bridge shell sample, the kinematic age distribution is consistent with that of the SMC population. This may suggest that the environmental conditions for the evolution of H<sub>I</sub> shells is similar in the two systems.

During a survey of SMC H<sub>I</sub> shells, Staveley-Smith et al. (1997) also found a large number of shells with ages that were too young to be conveniently related to a period of star formation triggered by the Magellanic cloud encounter. Under the assumption that H<sub>I</sub> shells are commonly driven by stellar winds, they suggest that as the Magellanic system is close to perigalacticon, it may be experiencing sufficient tidal disruption to stimulate a more recent period of star formation.

It is worth noting the assumptions made in calculating the kinematic age are not necessarily satisfied in every study. The equations used in this paper, as derived by Weaver et al. (1977), assume a homogeneous medium, and relate only to the expansion phase of the shell. The Magellanic Bridge can be seen to have structure and dynamics down to the smallest observed scales, and it is difficult to assess the extent to which the inhomogeneities affect the estimations of kinematic age and shell luminosity. The kinematic ages estimated in this paper are used more as means to compare between systems where data have been subjected to the same assumptions, rather than as a measure of the absolute age of the shell. Alternative models exist, and give rise to different estimates of the shell parameters. For example, a supernova model has been derived by Chevalier (1974). Using this model, the mean Magellanic Bridge shell energy is estimated to be  $\sim 5 \times 10^{49}$ , which is an order of magnitude larger than the estimates made using Weavers stellar wind model. The Weaver model has been used in studies of the SMC and H<sub>II</sub>, and to preserve some continuity, we have used it also in this study.

## 8 ALTERNATIVES TO THE STELLAR WIND MODEL

The lack of spatial correlation of the stellar population and the Shell population imply that other mechanisms may be operating to produce the observed spherical, expanding H<sub>I</sub> structures. These include energy depositions through

Gamma Ray Bursts (GRBs), High velocity Cloud impacts (HVCs) and ram pressure effects.

### 8.1 Gamma Ray Bursts

The origins of GRBs are not well understood, however, common models include the collisions of Neutron stars (e.g. Blinnikov et al. 1984) or the collapse of super-massive objects (Paczyński, 1998). These events can deposit  $\sim 10^{52}$  ergs into the ISM (Wijers et al., 1998),  $\sim 10$  per cent of which is imparted as kinetic energy into the local medium. Measurements of the gamma ray flux by Wijers et al. (1998), have led to an estimate of the probability of a GRB event of once per 40 million years per galaxy. These estimates assume that the GRB events release energy isotropically and without beaming, although beamed GRB events have been modelled to produce spherical structures after  $\sim 5$  Myr (Ayal & Piran 2001). If apply this probability estimate applies to the Magellanic Bridge, and assume the age of the Bridge is  $\sim 200$  Myr, as found by computer simulations (e.g. Gardiner, Sawa & Fujimoto 1994), we can estimate  $\sim 5$  Gamma ray Burst events since its creation. The number of shells found in the Bridge is clearly in excess of this, and there is no plausible way to justify the source of the majority of HI expanding features as GRB relics. However, caution should be taken when assuming the Magellanic Bridge will have the same kind of GRB frequency as a galaxy. The Bridge has a relatively small total mass, and it is likely to have a significantly lower Star formation rate. This, however, can only decrease the estimated GRB frequency. Additionally, the shell energies, as derived using both Weaver and Chevalier models, are three and two orders of magnitude respectively lower than the expected energy from a GRB. The low GRB frequency, and the insufficient shell energy suggest that GRB events are not a dominant mechanism for shell formation and expansion within the Magellanic Bridge.

### 8.2 HVCs

Simulations of HVC impacts into a galactic disk have been generated by Tenerio-Tagle et al (1986). Eight different scenarios were investigated, where the density, radius and velocity of the impacting HVC were varied. In general, it was found that HVCs of densities  $\sim 0.1 - 1 \text{ cm}^{-3}$ , impacting at  $300 \text{ km s}^{-1}$  were found to generate a spherical expanding void, with radii  $\sim 35-95 \text{ pc}$  after  $\sim 5$  Myr, and energies of  $\sim 10^{48-49}$ . More dense clouds, moving at higher velocities were capable of penetrating deeper into the gas disc and creating cylindrical holes of radii  $\sim 70 \text{ pc}$  in diameter after  $\sim 5$  Myr and depositing  $\sim 10^{49-51}$  ergs into the ISM. From Table 2, we see that the mean energy of the Magellanic Bridge shell population is more compatible with the former scenarios, however it should be borne in mind that this estimation of the shell energy is made assuming a stellar wind model, although certainly the radii of these simulations are consistent with those measured from the Magellanic Bridge shell population. It should also be noted that these simulated HVCs were impacting into a medium of density  $1 \text{ cm}^{-3}$ . The estimates of the Magellanic Bridge, from Section 2.4, are two orders of magnitude lower than this. We might therefore expect that an HVC cloud impact, such as the ones simulated by Tenerio-Tagle et al., would have a more destructive

effect than the simulations show. Such destructive impacts may not generate a complete, spherically expanding shell which would consequently be excluded from this survey. As such, although we can see from Fig.5 that the distribution of the surveyed HI expanding shells appears to be chiefly confined to regions of higher HI, we cannot confidently rule out this mechanism of shell formation for the entire Bridge shell population on the basis of this non-uniform distribution.

### 8.3 Ram Pressure

Bureau & Carignan (2002) have suggested that the stripping action of the intergalactic medium on infalling cluster members could also generate holes and tunnels. The feasibility of this hypothesis has been studied through simulations only tentatively, although with promising results. This model suffers from similar setbacks as the infalling HVC model in the case of the Magellanic Bridge: We would expect the distribution of the shells generated through this mechanism to be rather random, whereas the distribution of Magellanic Bridge shells is confined to high column density regions. The ram pressure model can not be said to be a primary cause of Magellanic Bridge expanding HI shells.

## 9 SUMMARY

High resolution HI maps of the inter-Magellanic Cloud region, the Magellanic Bridge, reveal a complex and intricate structure of lumps, filaments and holes across all observed scales, from  $\sim 98''$  to  $\sim 7''$ . In general, much of the HI of the Bridge appears to be confined into two velocity components at  $38 \text{ km s}^{-1}$  and  $8 \text{ km s}^{-1}$  [VGSR]. This bimodality converges to a single velocity of  $\sim 23 \text{ km s}^{-1}$  [VGSR] at  $\sim 2^h 20^m$ ,  $\sim 3.6 \text{ kpc}$  from the SMC towards the LMC. A large HI loop, approximately 1 kpc in diameter, can be seen in the Bridge, adjacent to the SMC.

A survey of HI spherical expanding shells of the Magellanic Bridge, has uncovered 163 examples of such structures. Generally, shells found within the Magellanic Bridge are less energetic, expand more slowly and are smaller than those found within the SMC, although this survey has shown that the mean kinematic age of shells in the Magellanic Bridge is approximately equivalent to that of the SMC. Although the HI column density and OB distribution seem to spatially correlate very well, as well as the distribution of HI expanding shell features and HI column density, we have found very poor correlation between the HI shells and OB association distributions in the Magellanic Bridge. In addition, there appears to be a local *excess* of HI immediately surrounding the positions of OB associations. These findings do not support the popular idea of stellar wind being the driving engine of an HI shell, although at this time there are no alternative shell-generation mechanisms that completely satisfactorily describe the energies and distribution of the observed shell population. The distribution of incomplete shell-like features of the Magellanic Bridge will be the focus of a future paper, and will help to ascertain the plausibility of the HVC model for shell generation mechanisms.

A comparison with other HI shell surveys of the Magellanic-type galaxies, the SMC and HoII, has shown that the survey appears to be insensitive to shells with large radii.

An examination of other HI surveys indicate that this survey used here was particularly rigorous in the definition of an expanding shell. As a result of the strictness of the selection criteria, we have found that a region of the Bridge, in which an excess of older shells exists, corresponds with a region of lower HI velocity dispersion. On the basis of this, we have suggested that shells are prone to fragmentation in a dynamic environment, where the tendency to fragmentation is somehow dependent on shell age and size. A future paper will focus on a census of incomplete and fragmented shell-like structures.

The only known H $\alpha$  shell in the Magellanic Bridge has been shown to be defined also in HI. This is the only HI shell that can be unmistakably be attributed to a stellar driving engine, and apart from it coincidence with the H $\alpha$  region, does not appear to have any other characteristics to distinguish it from the rest of the Magellanic Bridge shell sample.

## 10 ACKNOWLEDGEMENTS

The Authors would like to extend their thanks to the Referee for helpful advice and suggestions to improve this paper. Thanks also to Dr. Grahame White, Dr. Paul Jones, and also Dr. Raymond Haynes for their assistance in the 1997 ATCA observations. Finally, the Authors would like to acknowledge and thank the CSIRO and ATNF for time on the ATCA and Parkes Telescopes.

## REFERENCES

Ayal S., Piran T., 2001, AJ, 555, 23

Battinelli P., Demers S., 1998, AJ, 115, 1472

Battinelli P., Demers S., 1992, AJ, 104, 1458

Bica E.L.D., Schmitt H.R. 1995, ApJS, 101, 41

Blinnikov S.I., Novikov I.D., Perevodchikova T.V., Polnarev A.G., 1984, SvA. 10, L177

Brink, E., Bajaja E., 1986, A&A 169, 14

Bureau M., Carignan C., 2002, AJ, 123, 1316

Chevalier R.A., 1974, AJ, 188, 501

Demers S., Battinelli P., 1998, AJ 115, 154

Efremov Y.N., Elmegreen B.G., Hodge P.W., 1998, ApJ, 501, L163

Eklerova S., Palous J., Theis Ch., Hensler G., 1997, A&A, 328, 121

Eklerova S., Paulos J., 1996, A&A, 313, 478

Gardiner L.T., Sawa T., Fujimoto F., 1994, MNRAS, 226, 567

Gardiner L.T., Noguchi M., 1996, MNRAS 278, 191

Graham M.F., Smith R.J., Meaburn J., Bryce M., 2001, MNRAS 326, 539

Grondin L., Demers S., 1993, in Sasselov D.D. ed, The International Workshop on Luminous High-Latitude Stars, Astron. Soc. Pac., San Francisco, p. 380

Grondin L., Demers S., Kunkel W.E., 1992, AJ, 103, 1234

Cox D.P., 1972, ApJ, 179, 159

Hindman J.V., McGee R.X., Carter A.W.L., Kerr F.J., 1961, AJ, 66, 45

Kim S., Dopita M.S., Staveley-Smith L., Bessell M.S., 1999, AJ, 118, 2797

Lozinskaya T.A., 1992, in Supernovae and Stellar Wind in the Interstellar Medium, American Institute of Physics, New York, p.365

Mathewson D.S., Cleary M.N., Murray J.D., 1974, APJ, 190, 291

McGee R.X., Newton L.M., 1986, Proc. ASA, 6/4, 471

Mathewson D.S., Ford V.L., 1984, in Van Den Bergh S., de Boer K.S., eds, Proc. IAU Symp. 108, Structure and evolution of the Magellanic Clouds, D. Reidel Pub. Co. Holland, p.125

McClure-Griffiths N.M., Dickey J.M., Gaensler B.M., Green A.J., Haynes R.F., Wieringa M.H., 2000, AJ, 119, 2828

McCray R., Kafatos M., 1987, ApJ, 317, 190

McCray R., Snow T.P.Jr. 1979, ARA&A, 17, 213

Meaburn J. 1986, MNRAS, 223, 317

Oey M.S., Clarke C.J., 1997, MNRAS, 289, 570

Ott J., Walter F., Brinks E., Van Dyk S. D., Dirsch B., Klein U., 2001, AJ, 122

Paczyński B., 1998, AJ, 494, L45

Parker Q. 1998, in Johnston H., Ricketts S., eds, AAO Newsletter #87, Anglo Australian Observatory, p.8

Paturel G. et al., 1997, A&AS, 124, 109

Puche D., Westpfal D., Brinks E., Roy J-R., 1992, AJ, 103, 1841

Putman M.E., 2000, PASA, 17, 1

Putman M.E. et al., 1998, Nat., 394, 752

Brüns C., Kerp J., Staveley-Smith L. 2000, in Kraan-Korteweg R.C., Henning P.A., Andernach H., eds, IAU conf. proc. 218 Mapping the Hidden Universe: The Universe behind the Milky Way - The Universe in HI., Astron. Soc. Pac., San Francisco, p.349

Rhode, K.L., Salzer J.J., Wespahl D.J., Radice L.A., 1999, AJ, 118, 323

Sawa T.; Fujimoto M.; Kumai Y. 1999, in Chu, Y-H., Suntzeff N.B., Hesser J.E., Bohlender D.A., eds, IAU Symp. 190, New Views of the Magellanic Clouds, Astron. Soc. Pac. San Francisco, p.499

Shu F.H., 1992, in Osterbrock D.E., Miller, J.S., eds, The Physics of Astrophysics, University Science Books, Calif., p.264

Shull J.M., Saken J.M., 1995, ApJ, 444, 663

Stanimirović S., Lazarian A., 2001, ApJ, 551, L53

Stanimirović S., 2000, AA Soc. 197, #59.05

Stanimirović S., Staveley-Smith L., Dickey J.M., Sault R.J., Snowden S.L., 1999, MNRAS, 301, 417

Staveley-Smith L., Kim S., Putman M., Stanimirović S., 1998, in Schielicke R.E., ed, Rev. Mod. Astron. 11: Stars and Galaxies, Astronomische Gesellschaft, Hamburg, p.117

Staveley-Smith L., Sault R. J., Hatzidimitriou D., Kesteven M.J., McConnell D., 1997, MNRAS, 289, 225

Tenorio-Tagle G., 1981, A&A 94, 338

Tenorio-Tagle G. Franco J., Bodenheimer P., Rózyczka M. 1987, A&A 179, 219

Tenorio-Tagle Bodenheimer P., Rózyczka M., Franco J., 1986, A&A, 170, 107

Vishniac E.T., 1983, AJ, 274, 152

Walter F., Brinks E., 2001, AJ, 121, 6

Weaver R., McCray R., Castor J., Shapiro P., Moore R., 1977, ApJ, 218, 377

Wijers R.A.M.J., Bloom J.S., Bagla J.S., Natarajan P., 1998,

MNRAS, 294, L13 reference Wilcots E.M., Miller A.J.,  
1998, AJ, 116, 2363  
Zaritsky D., Harris J., Grebel E. K., Tompson I.B., 2000,  
APJ, 534, L53

This paper has been produced using the Royal Astronomical Society/Blackwell Science L<sup>A</sup>T<sub>E</sub>X style file.